Graduate Theses and Dissertations

Iowa State University Capstones, Theses and Dissertations

2011

Experimental study of low Reynolds number flow control devices: dynamic burst control plate and dynamic roughness

Travis Nicholas Grager
Iowa State University

Follow this and additional works at: https://lib.dr.iastate.edu/etd

Part of the Aerospace Engineering Commons

Experimental study of low Reynolds number flow control devices:

Dynamic burst control plate and dynamic roughness

by

Travis Grager

A thesis submitted to the graduate faculty

in partial fulfillment of the requirements for the degree of

MASTER OF SCIENCE

Major: Engineering Mechanics

Program of Study Committee:
Hui Hu, Co-Major Professor
Alric Rothmayer, Co-Major Professor
Terry Meyer

Iowa State University

Ames, Iowa

2011

Table of Contents

List of Figures

Abstract

Two experimental studies were conducted to investigate the use of surface actuation devices to suppress stall on a NACA 0012 airfoil by preventing the bursting of the low Reynolds number leading edge separation bubble. Both a leading edge burst control plate and a leading edge dynamic roughness field were studied as actuation devices. Through the use of pressure measurements, force measurements, and particle image velocimetry (PIV) data, it is shown that these devices have the ability to suppress the leading edge separation bubble at higher angles of attack than an airfoil without such devices. With the increased stall angle obtained through the use of these devices, lift performance is increased.

Chapter 1) Introduction

Low Reynolds number airfoil aerodynamics has been an area of great interest as micro aerial vehicles (MAV) have been seen as a very useful next generation of unmanned aerial vehicle (UAV). The extremely small size of these vehicles along with slow airspeeds places them in the low Reynolds number regime of 10^4-10^5.[1] For flows of Reynolds number at this scale and smaller, the physics are very different than those of higher Reynolds number flows that traditional manned aircraft experience. One of the predominant characteristics for this flow regime is the forming of a separation bubble near the leading edge of an airfoil at higher angles of attack.
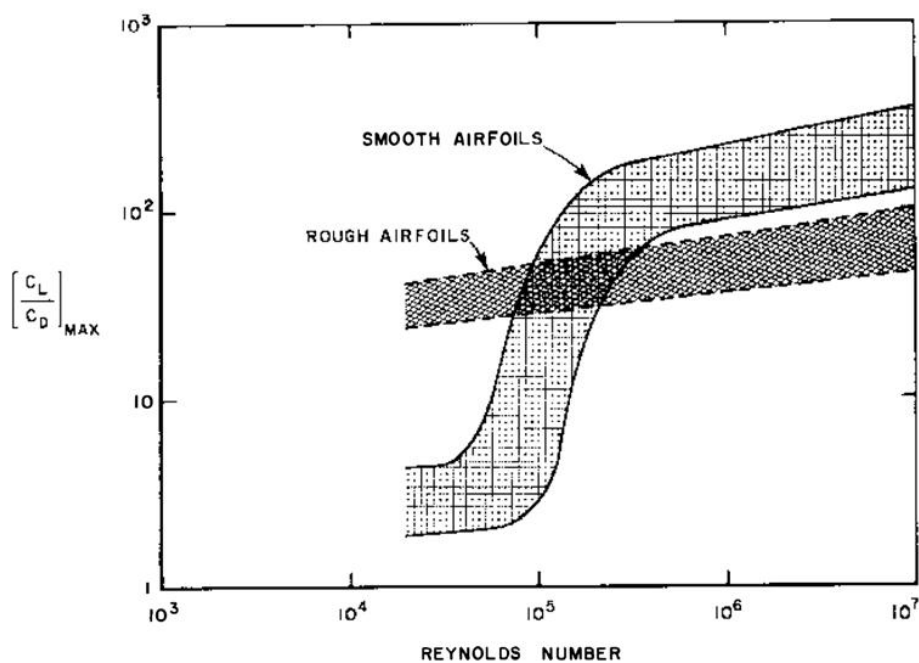
Figure 1: Low Reynolds number performance transition[3]

Many studies have been performed on the airfoil aerodynamics at low Reynolds numbers along with the correlation between the laminar boundary layer flow separation and the chord

Reynolds number as shown in Tani[1], Carmichael[2], Lissaman[3], Mueller[4], and Gad-el-Hak[5]. According to Lissaman[3], a separation bubble occurs when the boundary layer detaches from the surface of the airfoil and then reattaches further downstream as a turbulent boundary layer. The bubble size is predominantly influenced by the Reynolds number of the flow. Initially, a separation bubble can be relatively short, but any small disturbance such as an increase of the angle of attack can cause the bubble to burst and cover much of the upper surface of an airfoil causing a sudden stall and loss of performance. For chord Reynolds numbers below 5.0×10^4, the chord is too short for the separated boundary layer to reattach. At a chord Reynolds number of approximately 7.0×10^4, the chord is long enough for the separated boundary layer to reattach and form the leading edge separation bubble. Above a chord Reynolds number of 1.0×10^5, the bubble length is approximately 30-40% of the chord length. In general, the separation bubble's length is inversely proportional to the Reynolds number, thickness is proportional to its length, and the point of the laminar boundary layer separation is based on the angle of attack, not the Reynolds number. Flow measurements of the laminar separation bubble have been performed using different techniques including point wise measurements using laser Doppler velocimetry[6-8] and spatially resolved measurements such as PIV[9-12].
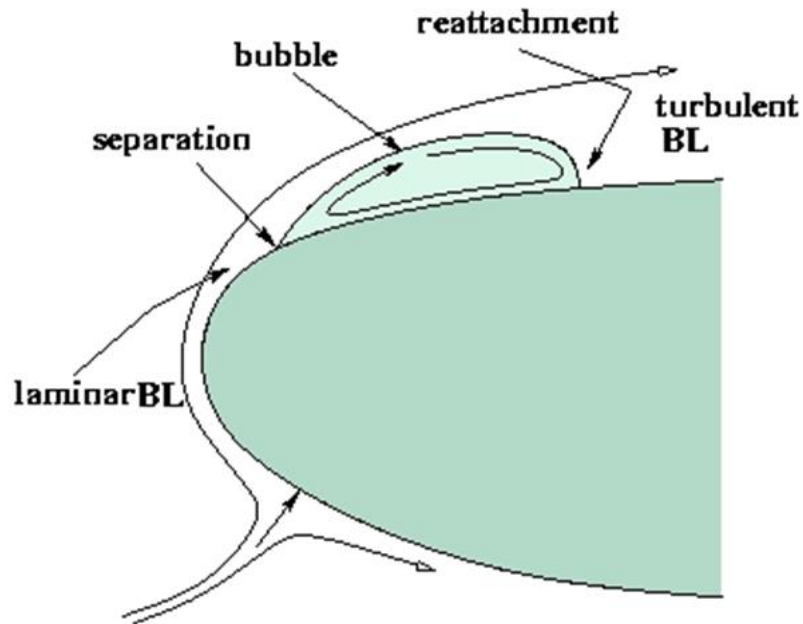
Figure 2: Leading edge separation bubble

Many studies have experimented with different methods to control the separation bubble and increase the angle of attack at which an airfoil will stall in this low Reynolds number regime. Most of the methods have examined ways to turbulate the boundary layer. Some of these methods include suction or injection of air into the boundary layer, static surface roughness, vibrating the surface, heating or cooling of the surface, and the use of micro-electro-mechanical systems. Rinoie et al.[13] suggested the use of a bubble burst control plate for the suppression of an airfoil stall. Their study found that by attaching a stationary small plate near the leading edge of a low Reynolds number airfoil could suppress stall and increase the lift performance by preventing the small separation bubble from bursting and forming a large separation bubble and eventually stall the wing. The first part of this thesis extends on the work of Rinoie et al.[13] by performing a preliminary investigation on the effects of a dynamic

burst control plate on stall suppression and increased airfoil performance at low Reynolds numbers.

Another study by Gall, Huebsch, and Rothmayer[14] looked at a similar method of small surface perturbations near the leading edge with the concept of dynamic roughness. Their study conducted both two-dimensional and three-dimensional simulations to show the effectiveness of dynamic roughness in breaking down a leading edge separation bubble. Along with the simulations, they produced an experimental model that helped validate their computational simulations. Key findings from their study were that the roughness heights could be as small as a few percent of the boundary layer thickness as long as the frequency was high enough, the dynamic roughness affects the flow similarly as static roughness when the frequency is too low, and that the roughness field does not need to start before the leading edge separation point to be able to still eliminate the separation bubble. The second part of this thesis extends on the research of Gall et al.[14] by performing further experimental studies on dynamic roughness through the use of PIV.

Chapter 2) Dynamic Burst Control Plate

Experimental Setup

This experimental study was conducted in the Bill James open-circuit wind tunnel located in the Aerospace Engineering Department of Iowa State University. The tunnel is capable of wind speeds up to 180 mph and has a test section that is 3 feet wide by 2.5 feet tall (914 by 762 mm). There are 13 screens located at the inlet of the tunnel followed by a 22:1 contraction ratio that help ensure laminar flow.

Model

The model tested was a straight, non-twisted wing with a NACA 0012 airfoil profile. The chord was $c = 300$ mm and the span $b = 585$ mm which resulted in an aspect ratio $AR \sim 2$. The incoming air velocity was 7 m/s which resulted in a chord Reynolds number $Re_c = 1.3$ x 10^5. End plates were attached to each span wise end of the model in order to reduce effects from the wind tunnel walls and any other three dimensional flow effects. An aluminum tube was installed through the half-chord of the model and was used for mounting the model in the center, both vertically and horizontally, of the test section. The model was rotated about this tube through an angle of attack, α, of 0° to 18°. In following the optimal bubble burst control plate sizing of Rinoie et al.[13] for a stationary burst control plate, an aluminum burst plate was located between $x/c = 0.05$ and $x/c = 0.075$ yielding a plate width $w_p = 7.5$ mm for the current model. Unlike Rinoie et al.[13], the current model's burst control plate is hinged at the leading edge of the plate so that it remains at the surface of the airfoil profile and allows the trailing edge to rotate from no deflection (standard NACA 0012 airfoil shape) to a nominal height of $h_p = 0.005c$ (1.5 mm) as shown in Fig. 3. An electric motor with an

elliptical cam shaft is mounted within the interior of the model to actuate the burst control plate. A spring is attached to the solid burst control plate in the interior of the model in order to keep it in contact with the cam. The elliptical shape of the cam produces a sinusoidal-like displacement.
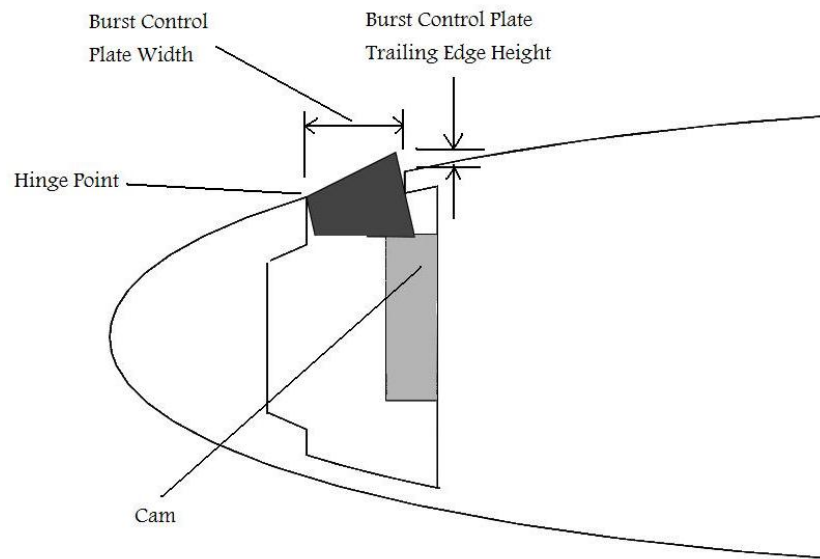
Figure 3:   Burst control plate actuation device
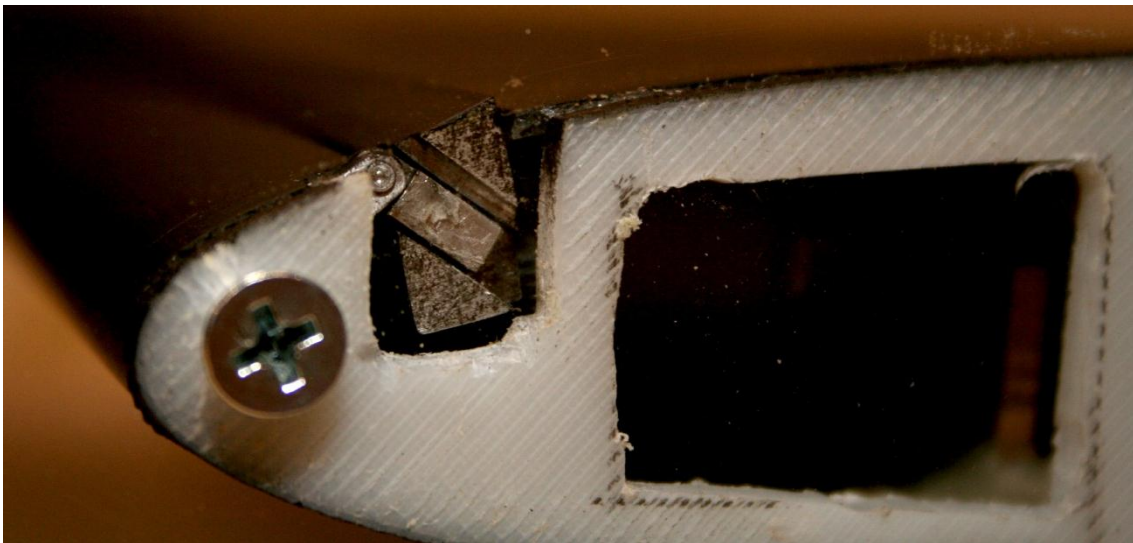
Figure 4:   Actual burst control plate

Instrumentation

Surface pressure data was collected at a total of 48 locations along the upper and lower surfaces. Electrical pressure transducers (DSA3217) were used to sample the pressure data at a rate of 400.6 Hz over a 30 second interval and were then averaged. Force measurements were also taken to verify the pressure data. Two JR3 30E12 multi-axis force/torque sensors were secured to the model to collect the force data. This data was obtained at a rate of 500 Hz over a time interval of 30 seconds and was then time averaged.

The experimental set-up is shown in Fig. 5 where the burst control plate model is mounted inverted to allow easy set-up of the laser for PIV data to be taken. A single CCD camera was used at a time for taking the 2D PIV images. Initial experiments used a 1392 x 1040 resolution CCD camera (PixelFly, Cooke Corp). Phase locked experiments used a 2048 x 2048 resolution CCD camera (PCO 2000, Cooke Corp). The flow was seeded with 1~5 micron oil droplets while illumination was provided by a double-pulsed Nd:YAG laser (NewWave Research Solo) adjusted on the second harmonic and emitting two laser pulses at a wavelength of 532 nm at a repetition rate of 4-10 Hz. The laser sheet was created by passing the laser beam through a set of spherical and cylindrical lenses and aligned with a mirror. The laser sheet was positioned near the center span of the model and had a thickness of approximately 2 mm. The triggering of the laser and camera was controlled via a digital delay generator (Berkeley Nucleonics, Model 565).
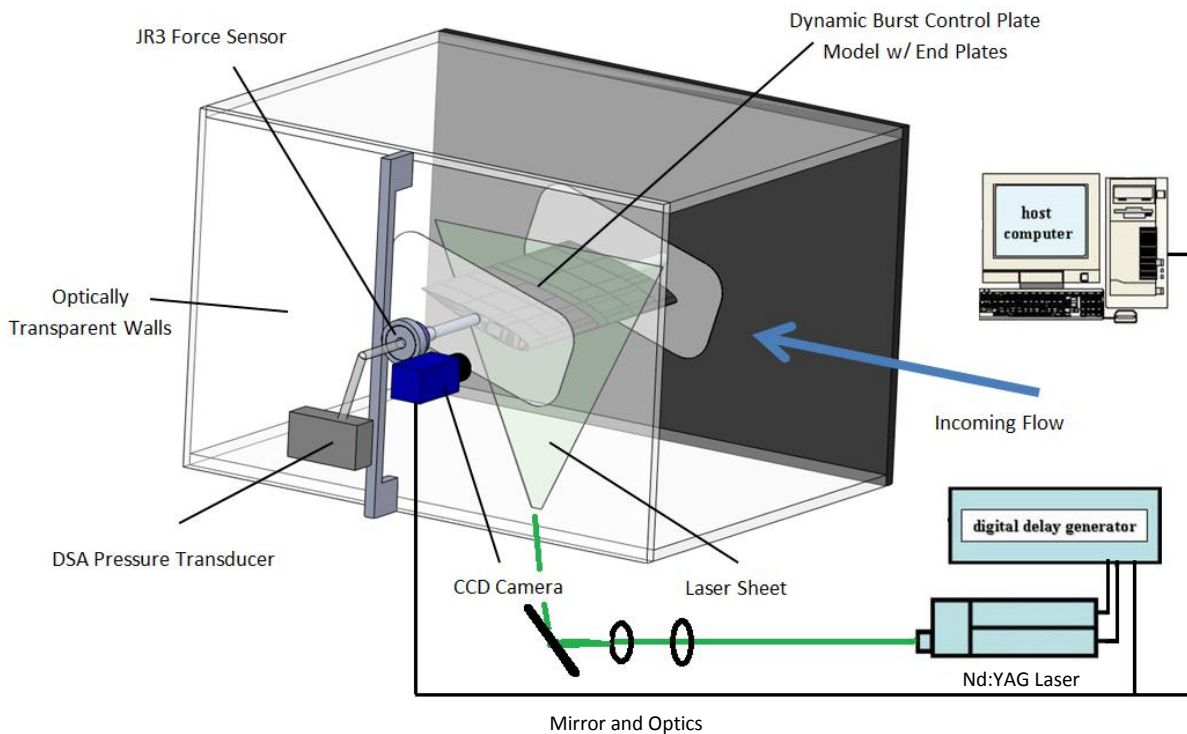
Figure 5: Burst control plate experimental setup

Test Cases

Preliminarily, five different test conditions were tested in which pressure, force, and both wide and zoomed view PIV data were taken. A 'smooth' case which represents the standard NACA 0012 airfoil profile, i.e. no deflection of the burst control plate, used as a control as the model is not a perfect NACA 0012 profile near the burst control plate, a 'stationary' case that has the burst control plate held in the maximum deflection position, and three dynamic cases in which the plate was actuated at 30, 60, and 120 Hz. A laser tachometer was used to measure the speed of the motor and thus, in turn, the frequency at which the burst control plate was actuated. Due to instabilities on the load of the motor, the frequencies varied +/- 6 Hz of their nominal value. Although initial testing of the burst control plate yielded full deflection response (no deflection up to full deflection), testing within the wind tunnel did

not have the burst control plate returning to the no deflection position, instead it vibrated about a slightly deflected position.

A 'phase-locked' case was then tested at a vibration frequency of 20 Hz for an angle of attack of 13°. A second digital delay generator was combined with the PIV system to trigger the data acquisition based on the position of the burst control plate. As the plate was not vibrating at the exact frequency of the motor, an extension was attached to the burst control plate, next to the far end plate, which would magnify the moment arm and allow the laser tachometer to be triggered when the plate was fully deflected. The laser tachometer then sent a trigger to the added delay generator which would then add a predetermined delay before triggering the PIV system in order to obtain images at eight different positions of the burst plate. These eight positions, or phases that are 45° apart with the minimal deflection ($\Phi=0^o$), three equally spaced phase angles up to full deflection ($\Phi=180^o$), and then three phase angles until returning to minimal deflection. A frequency of 20 Hz was tested as it provided a larger change in burst control plate deflection height and reached a more stable vibrational frequency in comparison to the higher frequencies. Pressure data was also collected at this lower frequency and verified that the forces produced matched those found at the higher frequencies for this angle of attack.
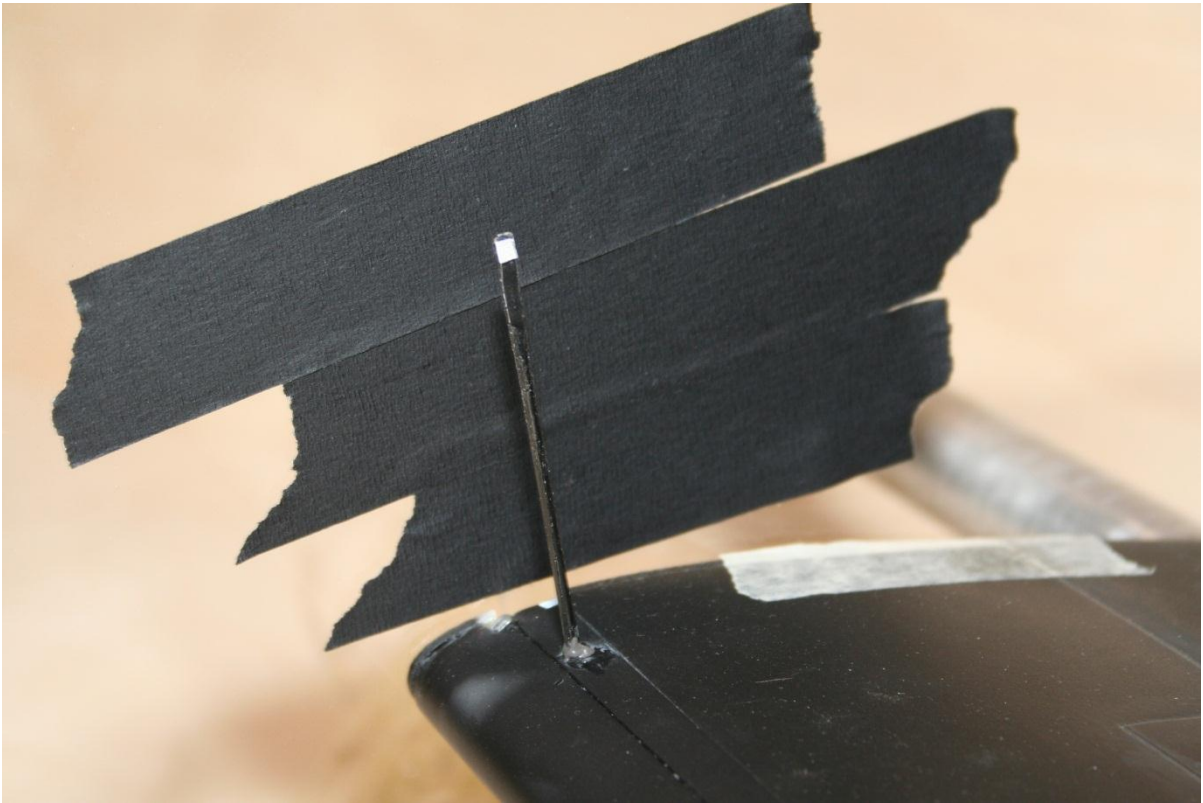
Figure 6: Extension from burst control plate for triggering

Results and Discussion

Pressure Distributions

Pressure distribution plots are shown in Fig. 7 for angles of attack of 12° to 15° in increments of one degree. From these plots, it can be seen that at 12° the distributions for all cases overlap one another which is expected from the lift curve. At 13°, the 'smooth' and 'stationary' cases both begin to stall while the dynamic cases do not. The dynamic cases at this angle show the traditional pressure distribution curve plateau near the leading edge due to a short separation bubble. This trend continues for an angle of attack of 14°, before the dynamic burst plate effects start to deteriorate at 15°. At 14°, the 30 Hz case forms a pressure distribution profile similar to that of a long leading edge separation bubble before stalling at 15°.
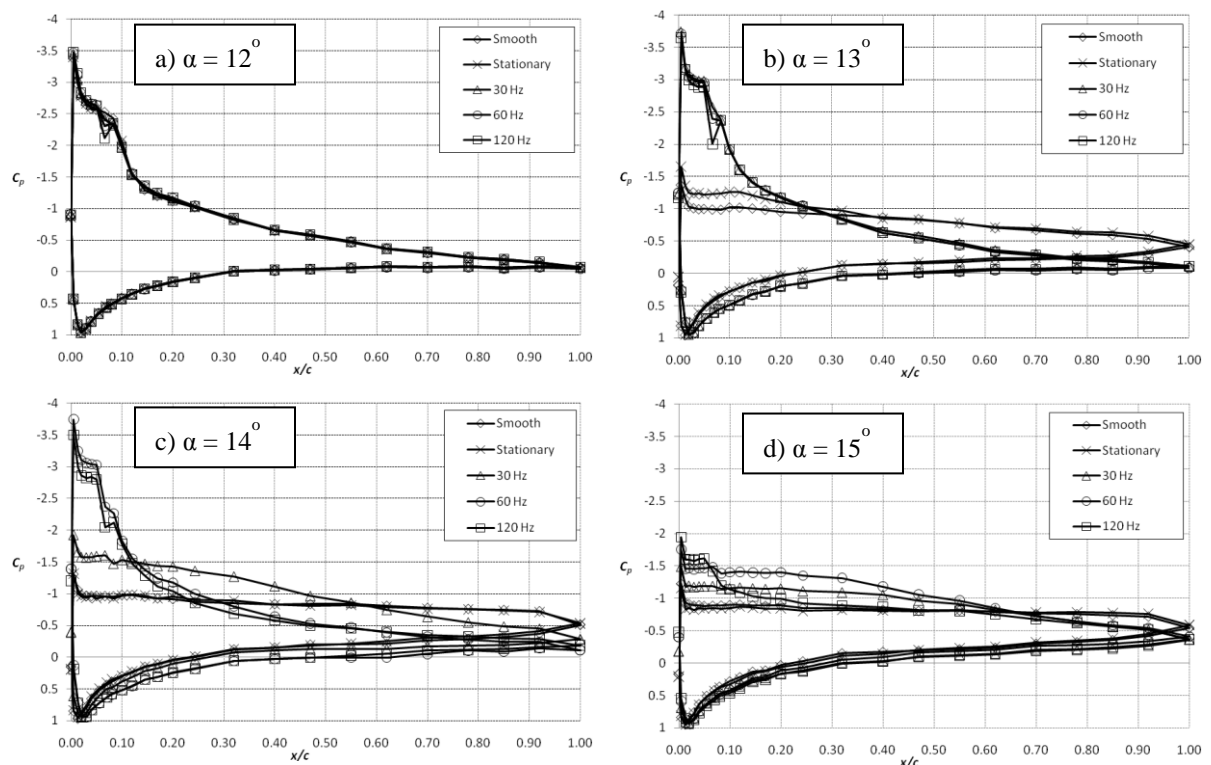
Figure 7:   Pressure coefficient distribution *a) α=12°, b) α=13°, c) α=14°, d) α=15°*

Lift Characteristics

The lift characteristics are presented in lift coefficient (C_l) versus angle of attack (α) curves shown in Fig. 8 & 9. Figure 8 was calculated from the integration of the pressure distribution while Fig. 9 was calculated from the force measurements which include three-dimensional effects. The two methods agree well for the "smooth" case and for the increased effectiveness of a dynamic burst control plate at delaying stall and providing more lift over the 'smooth' and 'stationary' cases. However, the force measurement results provide a much smoother stall region than that of the pressure measurement results.

Unlike Rinoie et al. [13], the 'stationary' case does not show much improvement in the maximum lift coefficient obtained over the standard airfoil, and neither does it delay the stall angle as much. These differences can be accounted in that the 'smooth' case that is used as the reference case in this study has slight perturbations from the standard NACA 0012 airfoil near the burst control plate which can act as a trip and turbulate the boundary layer. For this reason, the exact lift performance increase of the dynamic burst control plate can not be compared to the standard NACA 0012 airfoil, but can only be compared to a stationary dynamic burst control plate.
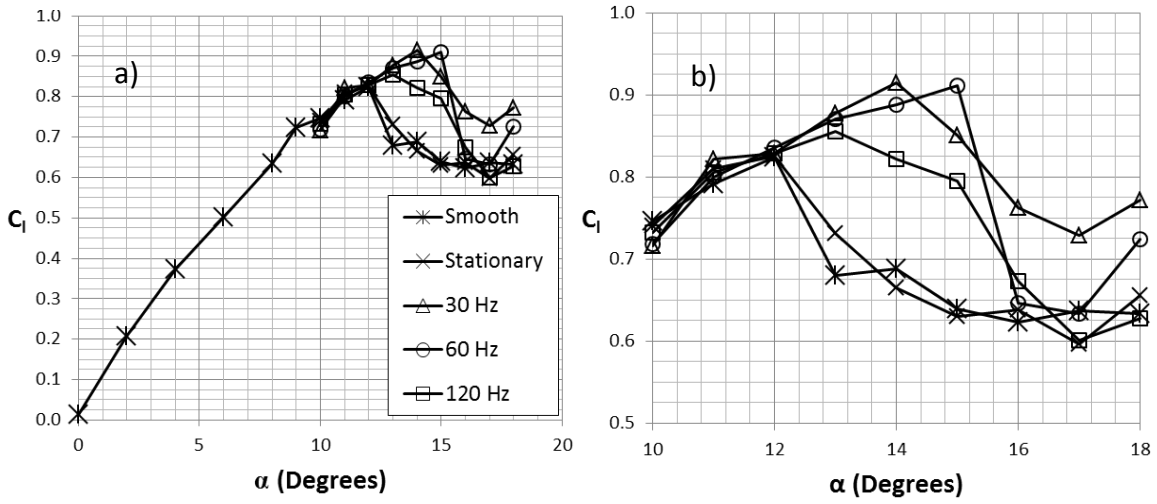
Figure 8: Lift curve based on pressure measurements *a) entire lift curve, b) magnified stall region*
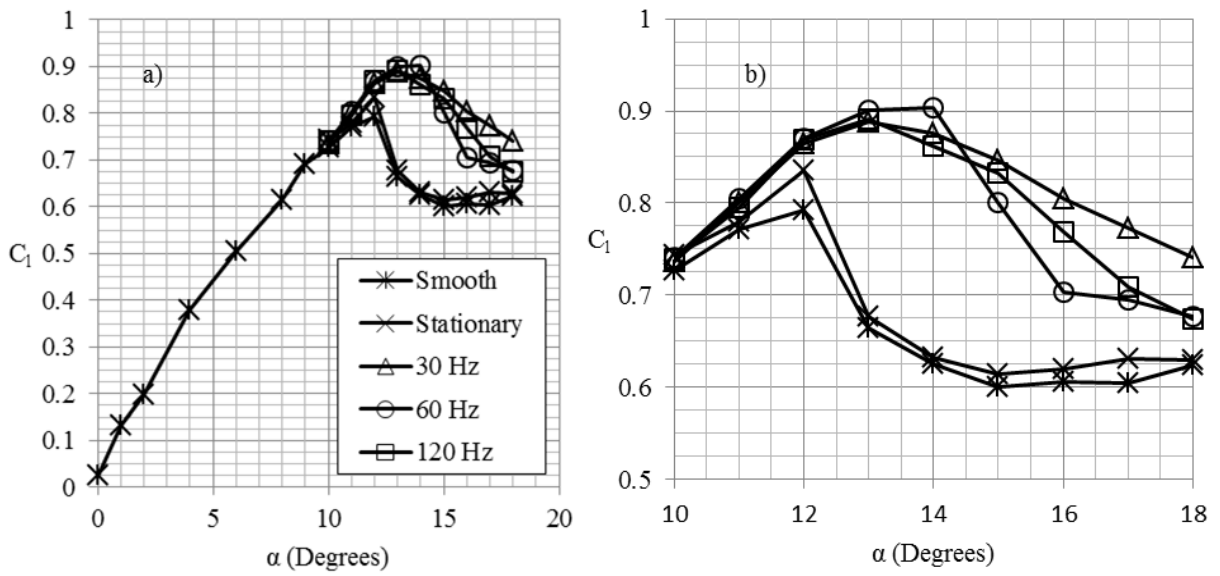
Figure 9: Lift curve based on force measurements *a) entire lift curve, b) magnified stall region*

Ensemble Average PIV Data

The ensemble average PIV data is provided in the following three figures. Figure 10 shows contours of the ensemble average normalized velocity magnitude ($|V|$) for the largest field of data recorded. This figure serves simply as evidence of suppression of stall by the addition of dynamically operating the burst control plate over the use of a stationary burst control plate which has a large separation zone. Large differences in the velocities near and far from the airfoil surface along with reflections that could not be removed in the captured images for these cases also cause these contours only to be used as basic evidence and that a more zoomed in view must be used for further examination.
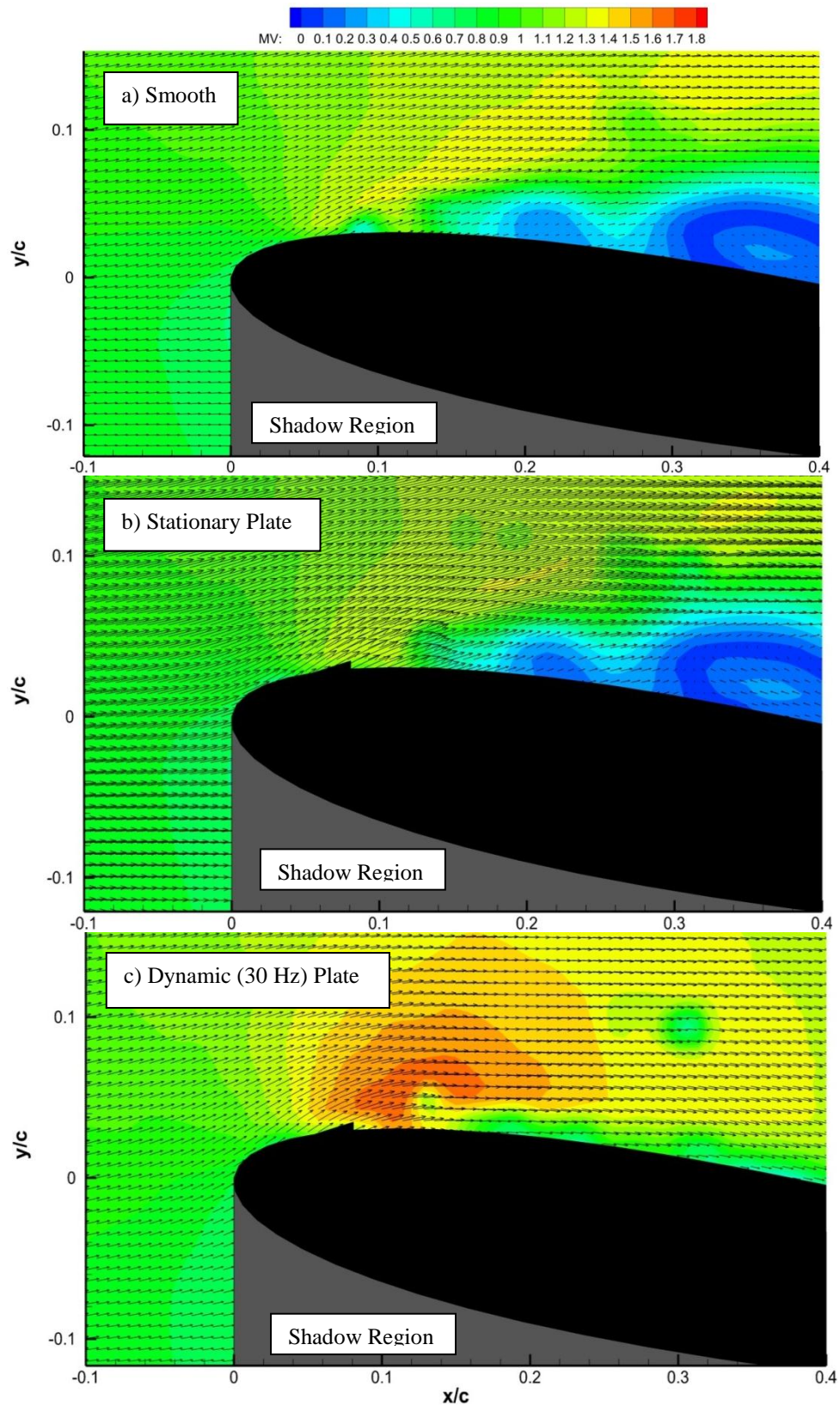
Figure 10: **Wide view ensemble average normalized velocity magnitude contours.** *a) smooth airfoil, b) stationary burst control plate, c) dynamic burst control plate operating at 30 Hz*
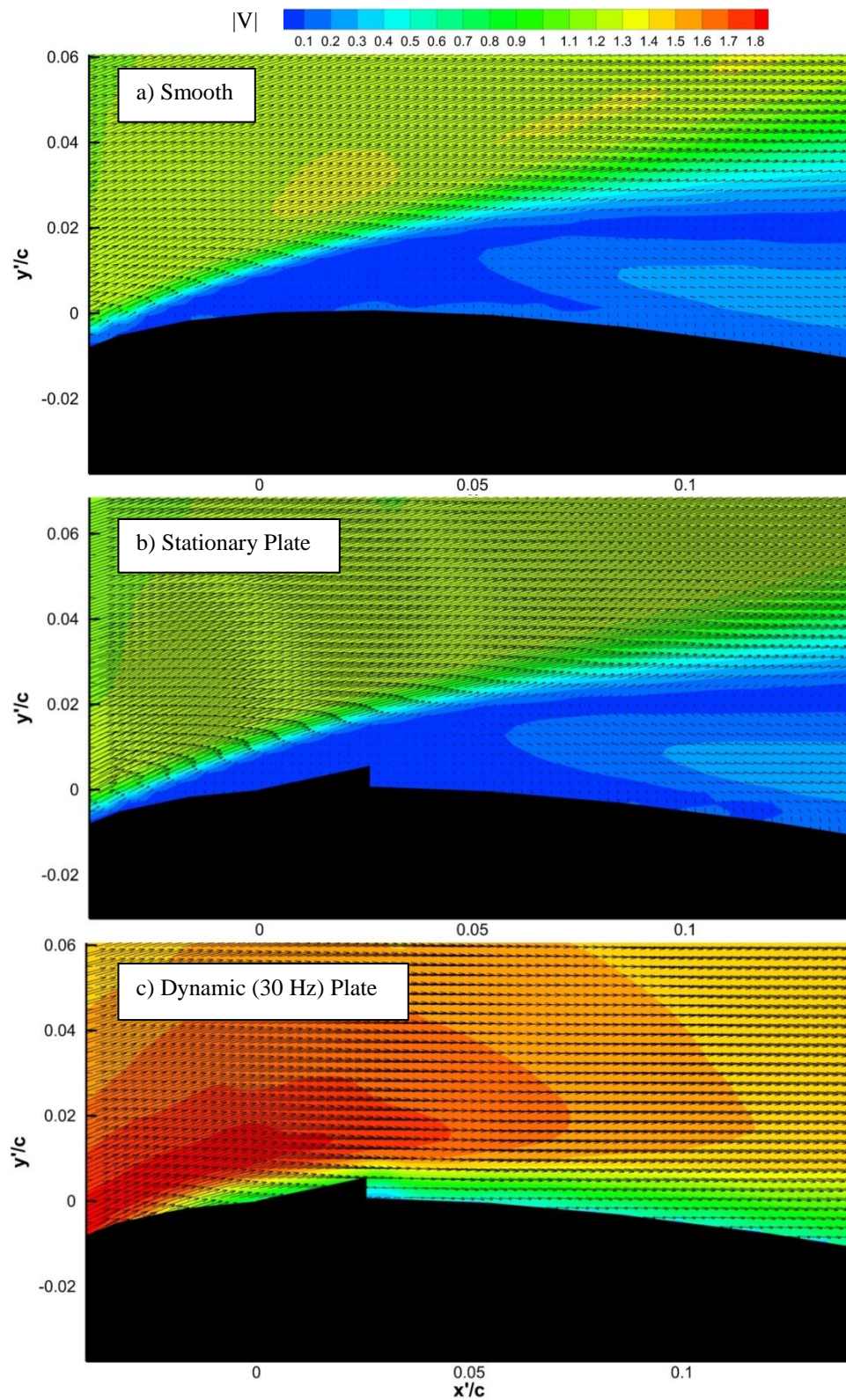
Figure 11: **Zoom view ensemble average normalized velocity magnitude contours.** *a) smooth airfoil, b) stationary burst control plate, c) dynamic burst control plate operating at 30 Hz*
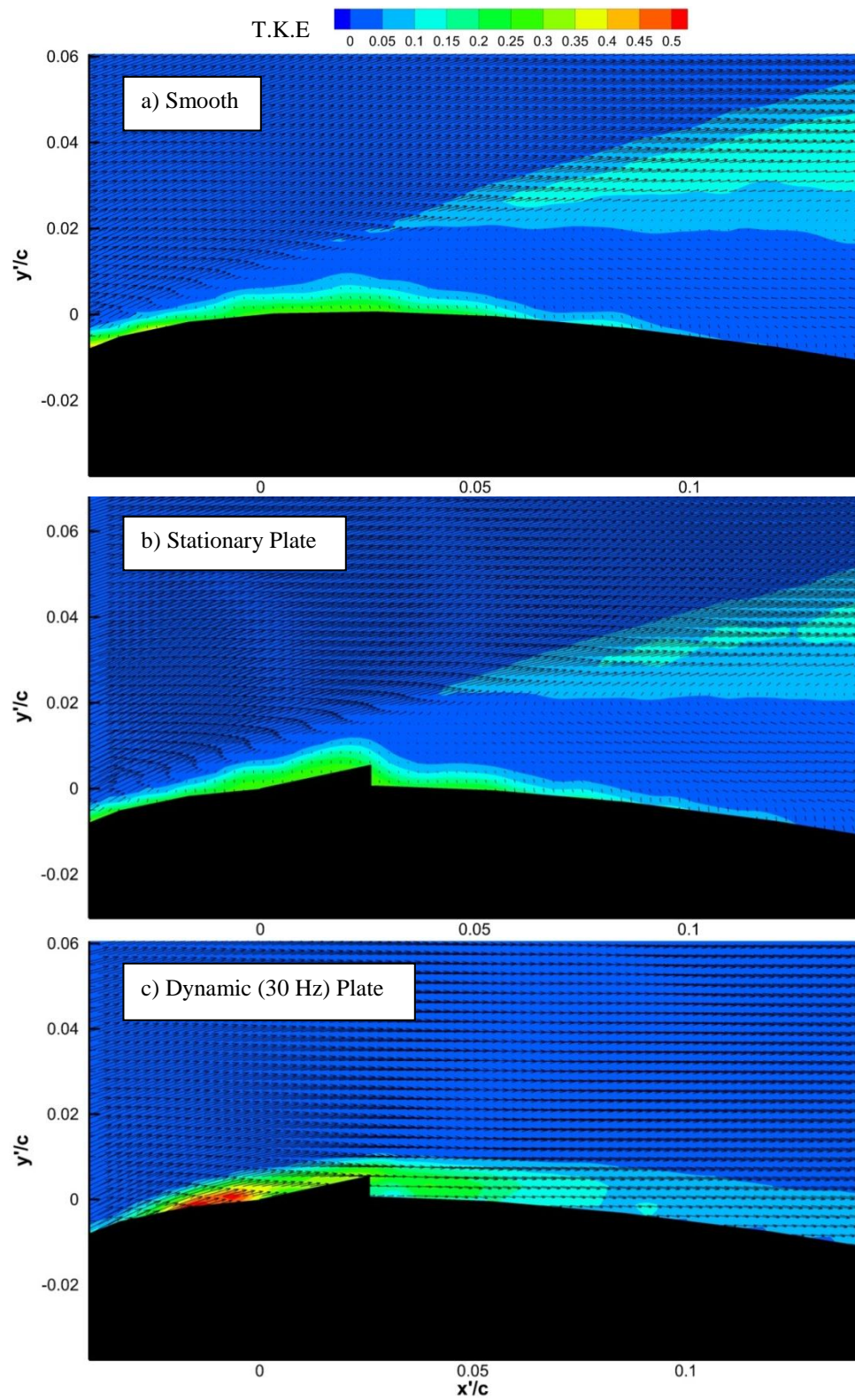
Figure 12: Zoom view of normalized turbulent kinetic energy (T.K.E.) contours. *a) smooth airfoil, b) stationary burst control plate, c) dynamic burst control plate operating at 30 Hz*

Figure 11 shows a magnified view of the flow in the vicintity of the burst control plate. (Note: The coordinate system has changed from x/c which is centered about the leading edge of the airfoil to x'/c which is centered about the front of the burst control plate for the zoomed in cases.) From these contours, it can be clearly seen that the boundary layer separates ahead of the burst control plate and forms a shear layer for the stationary case while it reattaches just beyond the burst control plate in the dynamic case.

To help understand the means in which the shear layer created by the leading edge separation bubble reattaches to the airfoil surface, contours of the normalized turbulent kinetic energy (T.K.E) are shown in Fig. 12. It is evident in both cases that there is an area of strong T.K.E surrounding the burst control plate, but in the dynamic case, there is a much stronger portion just ahead of the plate. This stronger area of T.K.E. seems responsible for a thinning of the shear layer and adding energy to cause reattachment.

Phase Average PIV Data

The phase average results from the PIV data were difficult to interpret what changes were happening in the flow. To assist in gaining a better understanding of the flow differences between each phase, an ensemble average velocity contour was obtained from a non-phase locked case and was subtracted from each phases' average velocity contour to obtain the phase average induced velocity as well as the phase average induced vorticity. The normalized induced vorticity (ω^i_z) contours and induced velocity vectors for the eight phases are found in Fig. 13. The first phase ($\Phi = 0^o$) represents the burst control plate in the lowest position. The phase angle increases from this location in 45° increments until it reaches the

maximum deflection point ($\Phi = 180^{\text{o}}$) at which point it changes direction and starts decreasing in deflection with an increasing phase angle until it reaches the minimum displacement point again.

It can be seen from the normalized induced vorticity contours that at the maximum deflection position (Fig. 13e), the induced vorticity along the shear layer is the highest allowing for a strong reattachment. In comparison to the rest of the phases, this phase, where the plate transitions from ascending to descending, seems to be the dominant mechanism in the reattachment process. Although there is some correlation in the flow pattern from phase to phase, there is a lot of noise within these contours. This noise could possibly be due to instability within the phase lock due to the vibrational frequency varying and errors in accurate triggering of the PIV system.
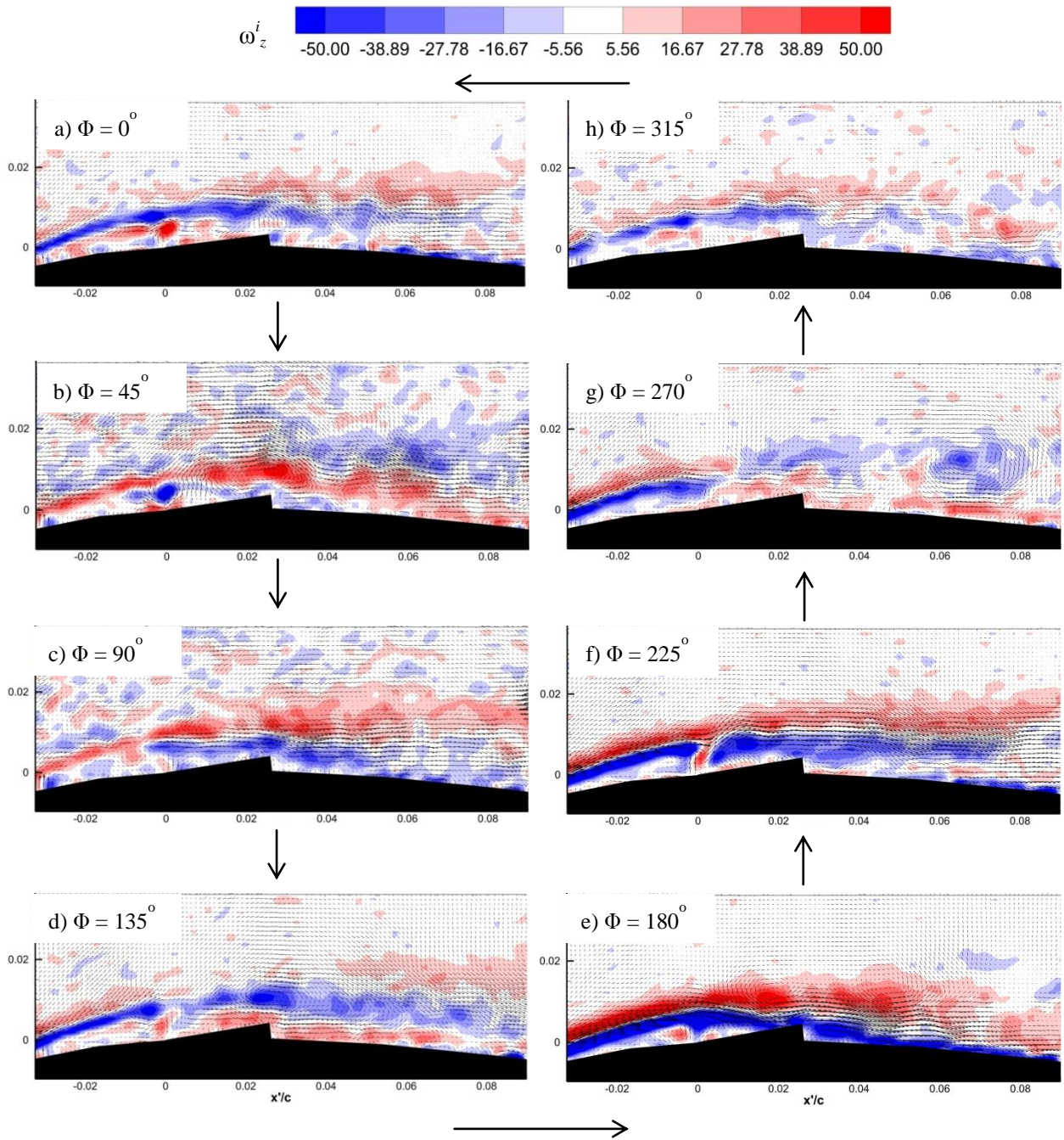
Figure 13: Phase average spanwise induced vorticity contours *a) Φ=0ᵒ (minimal deflection), b) Φ=45ᵒ (1/4 deflection on upstroke), c) Φ=90ᵒ (1/2 deflection on upstroke), d) Φ=135ᵒ (3/4 deflection on upstroke), e) Φ=180ᵒ (maximum deflection), f) Φ=225ᵒ (3/4 deflection on downstroke), g) Φ=270ᵒ (1/2 deflection on downstroke), h) Φ=315ᵒ (1/4 deflection on downstroke)*

Conclusion

An experimental investigation was performed on the performance of a dynamic burst control plate compared to a stationary burst control plate. It was found that the vibration added to the burst control plate increases the turbulent kinetic energy in the vicinity of it and forces the shear layer to reattach to the airfoil surface. Phase averaged results of the induced vorticity possibly indicate that the transition between the upstroke and down stroke of the burst control plate is the leading force in creating the additional turbulence needed to reattach the shear layer to the airfoil surface.

Chapter 3) Dynamic Roughness

Experimental Setup

This experimental study was conducted in a closed-circuit wind tunnel located in the Aerospace Engineering Department of Iowa State University. The tunnel is capable of wind speeds up to 150 mph and has a test section that has a 12 x 12 inch (304 x 304 mm) cross section with transparent walls. Installed ahead of the test section are a series of screens and a honeycomb structure followed by a contraction section which help provide uniform, low turbulence flow to the test section. The standard deviation of velocity fluctuations for the incoming flow was found to be 0.8% of the free stream velocity as measured by a hotwire anemometer.

Model

The model tested was a straight, non-twisted wing with a NACA 0012 airfoil profile. The chord was $c = 150$ mm and the span $b = 300$ mm which resulted in an aspect ratio $AR = 2$. The incoming air velocity was set for 2.7, 5.3, 7.8, and 10.4 m/s which resulted in chord Reynolds numbers (Re_c) of 2.5 x 10^4, 4.9 x 10^4, 7.3 x 10^4, and 9.7 x 10^4 respectively.

The model (Fig. 14 & 15) was designed using the 3D CAD program SolidWorks and printed using the Objet Alaris 3D printer. The printer's extremely high accuracy, fine resolution, very thin layer thickness (28 micron), and method of printing with continually curing layers produces a very accurate model with the ability for airtight pressure taps to be printed within it. The high accuracy also allowed for the model to be printed in multiple sections and assembled. It was chosen to print the model in three main sections: a leading edge dynamic

roughness section, an outer section that the leading edge mounts to, and the tunnel mounting section.
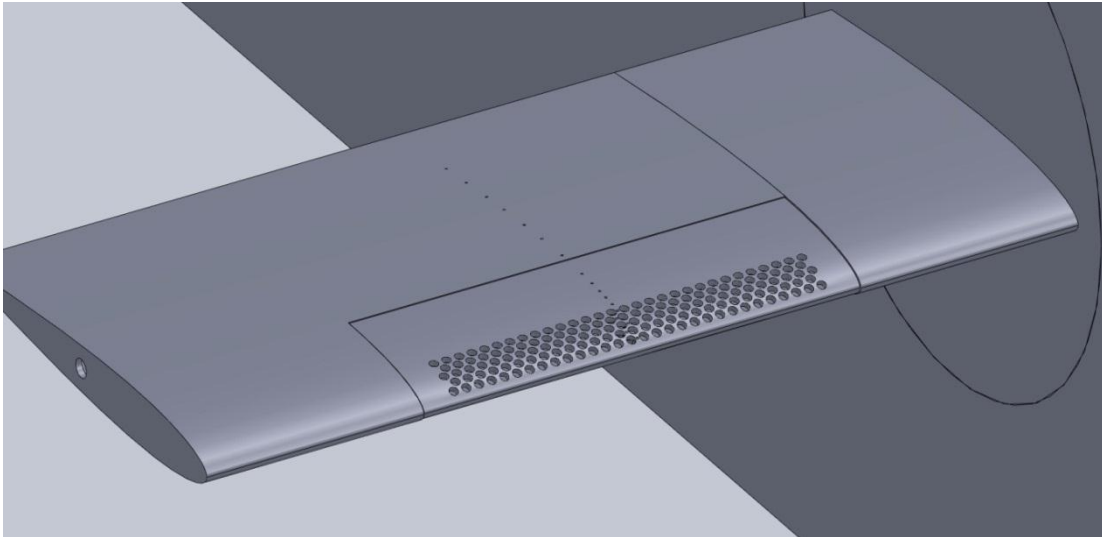
Figure 14:   CAD rendering of dynamic roughness model
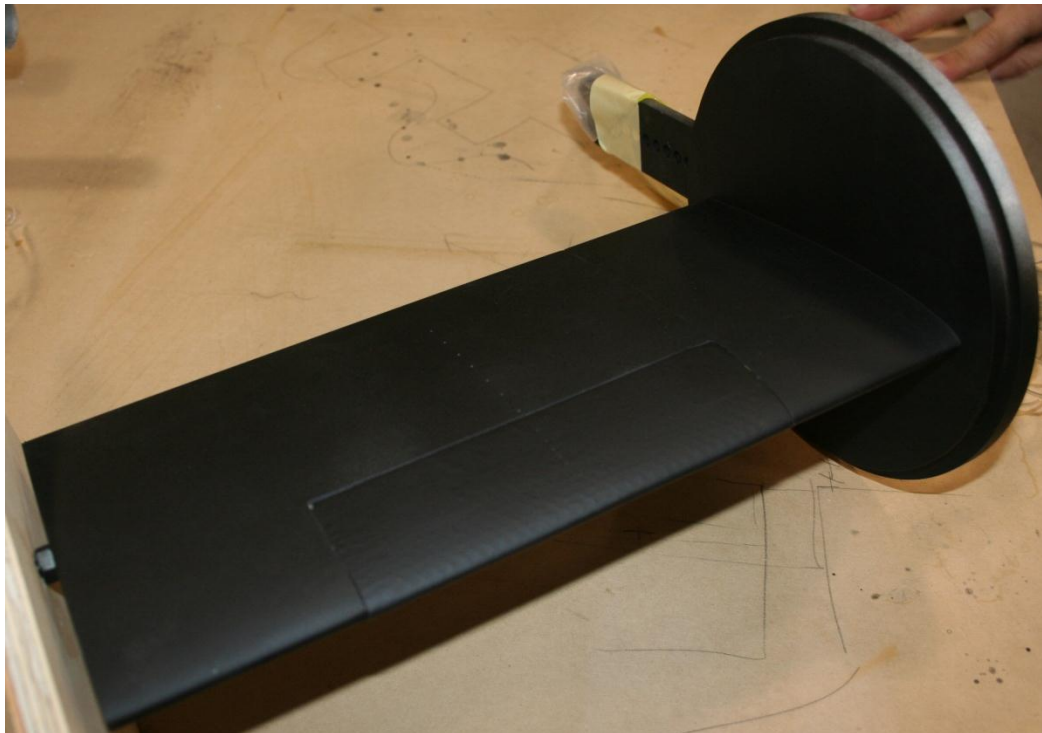
Figure 15:   Finished dynamic roughness model

The leading edge dynamic roughness section has a span that is half of that of the entire model and has a width of only 30% chord. Attached over the entire surface of the dynamic roughness section is a thin layer (.006 in) of latex rubber that is painted with a black rubber plastic for PIV measurements as shown in Fig. 17. This section was printed in one piece so that the inside of the model could be a hollow airtight chamber with holes only where dynamic roughness elements are located. With the latex covering these holes, when the chamber is pressurized, the latex forms a small round bump on the surface creating a roughness element. Cycles of pressurizing and depressurizing the chamber cause the roughness elements to form and flatten creating dynamic roughness. The dynamic roughness region starts at 1.07% chord and ends at 10.76% chord. The roughness elements (example shown in Fig. 18) are 2% chord (3 mm) diameter at the base and a max height of 0.15% chord (230 micron). Elements are arranged so that they are spaced 1.46 diameters center-to-center in the spanwise direction and aligned in the streamwise direction in such a manner that the front edge of a row of elements aligns with the back edge of the elements in front of it. Rows of elements are positioned in an alternating pattern as shown in Fig. 16. Pressure taps were also printed within the model including throughout the dynamic roughness region (see smaller holes in Fig. 16). There were a total of 35 pressure taps, of which 20 were located in the leading edge section, with diameters of 0.8 mm printed into the model.
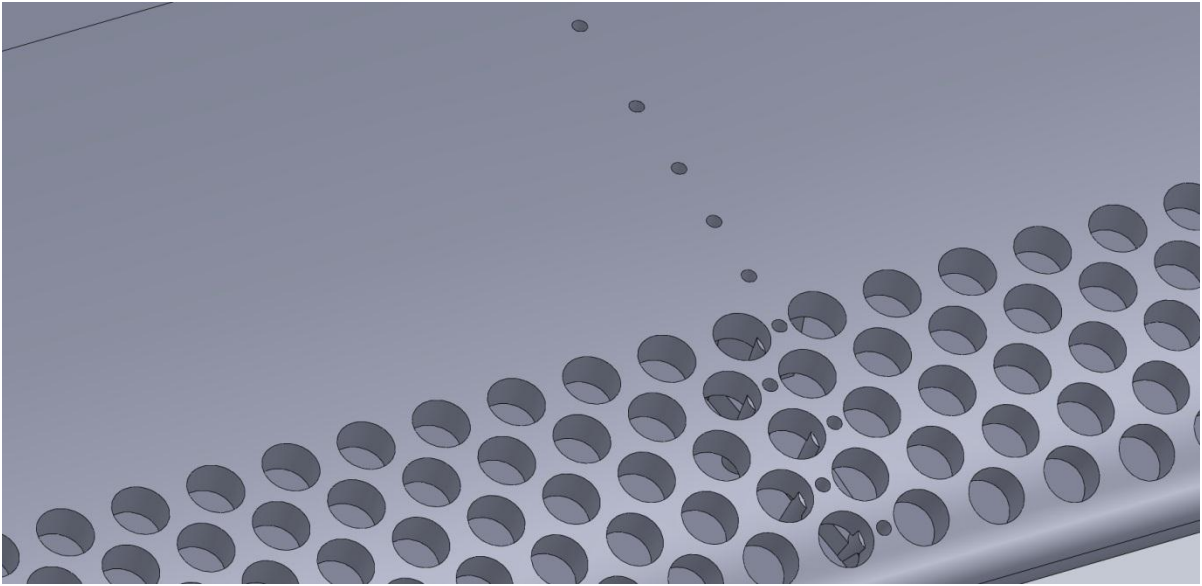
Figure 16:   CAD rendering of leading edge roughness holes and pressure taps
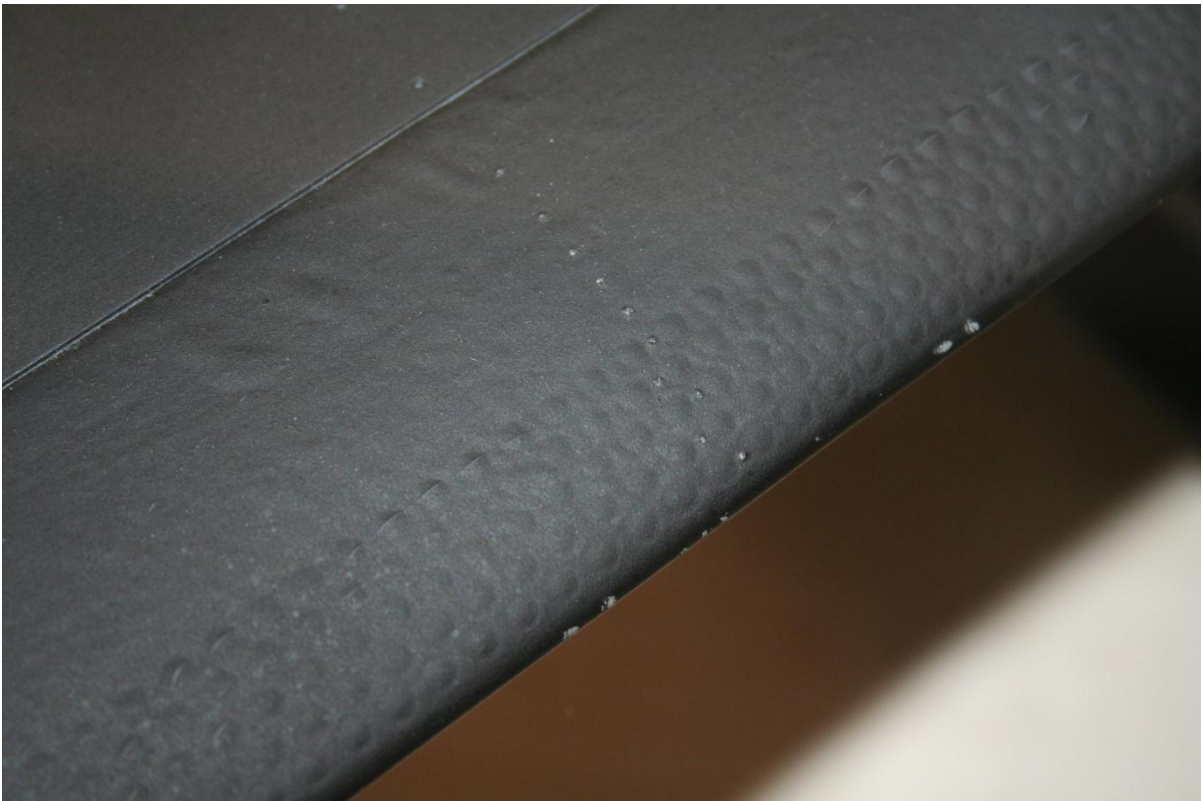
Figure 17:   Finished leading edge with latex covering
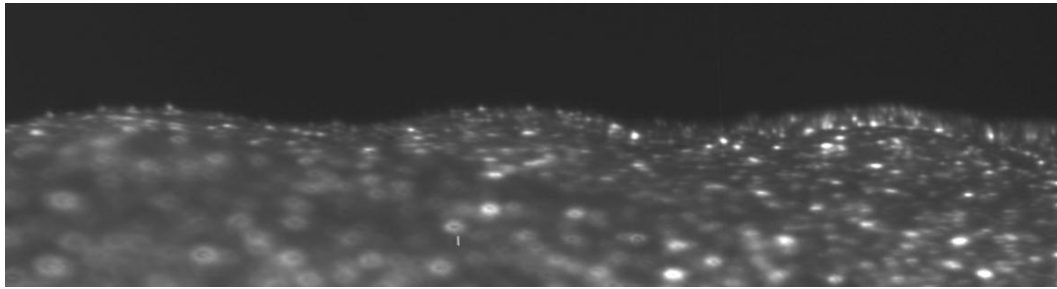
Figure 18: Dynamic roughness elements fully deflected

The leading edge section slid into a slot that aligned it with the outer section and held it into place. The outer section was printed as an upper and lower half with internal ribbing and support structures.   Pressure taps were connected internally and then run out of the model. A threaded rod located at half chord was attached within the outer section of the model and extended outside of it on both ends. On the side furthest from the mount, it was used as a pivot point for adjusting angle of attack and served as a structural support for securing the mount section of the model.
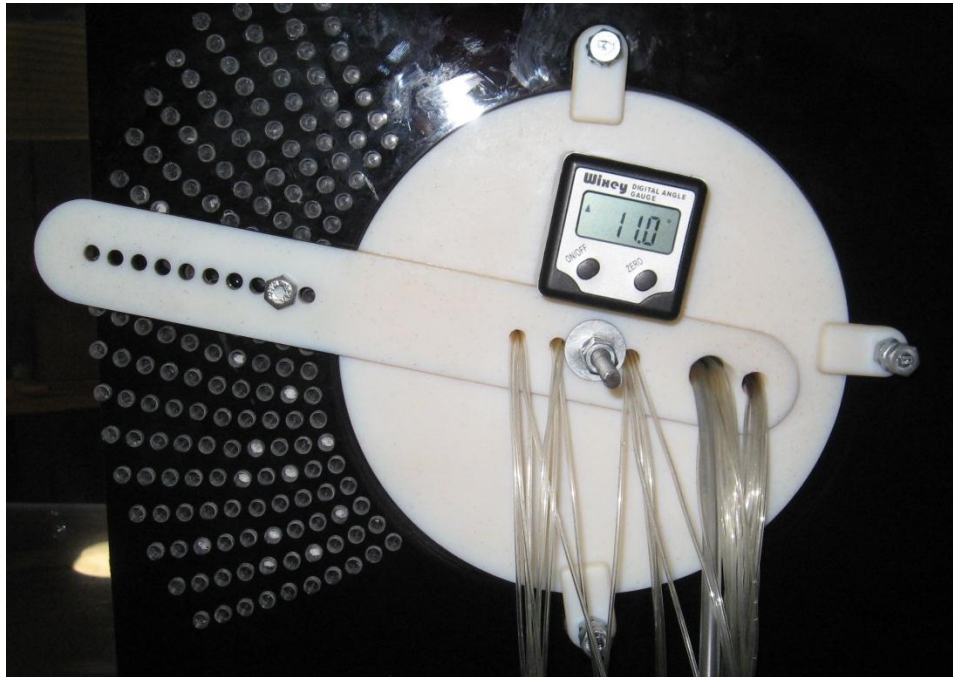
Figure 19:   Tunnel mount with angle of attack adjustment

The mount side of the model connected the model to the back wall of the wind tunnel. This section consisted of a quarter of the airfoil as well as a solid circular wall portion which served as part of the tunnel wall. The circular wall portion of this section had a rabbet placed on it to align the model with a hole built into the tunnel wall.   Three capture screws were used to tighten this section to the tunnel wall and hold it in place. Additionally there was an arm incorporated on the outside portion of this section that was aligned with the chord line of the airfoil. This arm had ten holes located at different radii from the center of the airfoil. A series of holes tapped in the tunnel wall in the pattern similar to a machinist indexing head allowed the model to be easily and accurately set to different angles of attack in half degree increments; this can be seen in Fig. 19.

Actuation Pump

The dynamic roughness region's air chamber was pressurized and depressurized through the use of a novel pump which was created using COTS (commercial off the shelf) parts. This system is shown in Fig. 20. A two cycle 90 cubic centimeter remote control aircraft engine served as a pump while a ½ horsepower variable speed electric motor was used to drive the aircraft engine. A set of pulleys and a belt were used to connect the motor to the engine. Copper pipe fittings were attached to the head of the motor. These fittings allowed the pressure supplied to the model to be crudely controlled through the use of a needle valve which would siphon off some of the air before it would reach the hose that was attached to the model. Controlling the pressure allowed control of the maximum height of the roughness elements. A laser tachometer was used to verify the drive frequency of the engine which was controlled to the nearest 0.5 Hz. The system was able to produce pumping frequencies up to 92 Hz.
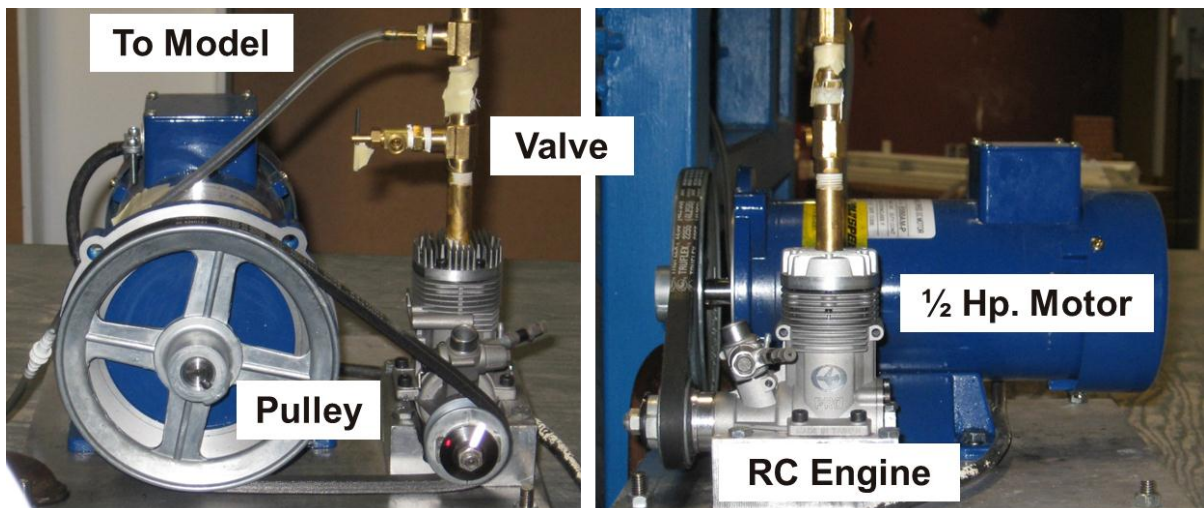
Figure 20:   Actuation pump system
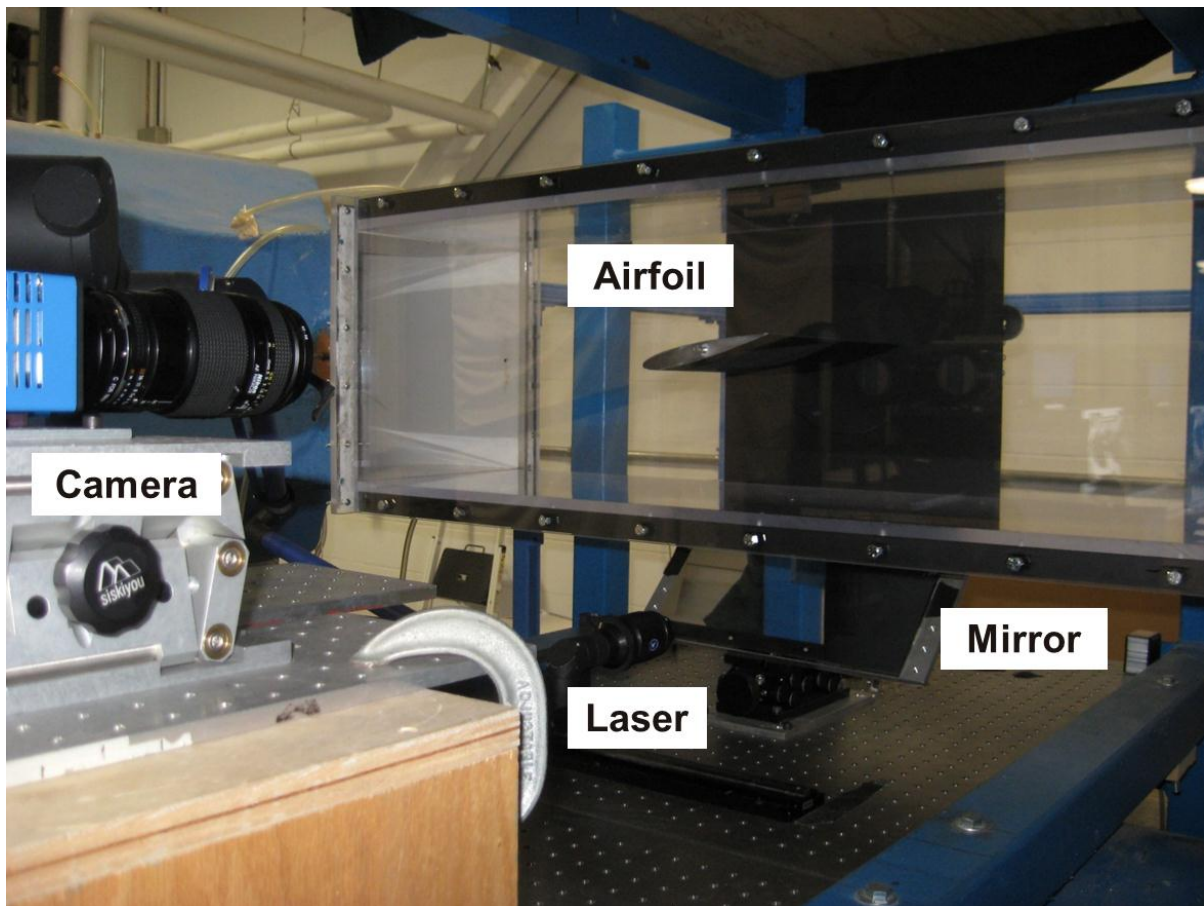
Figure 21: Experimental set-up

Instrumentation

The experimental set-up with the same basic set-up as the burst control plate study is shown

in Fig. 21 where the dynamic roughness model is mounted inverted to allow easy set-up of

the laser for PIV data to be taken. Two CCD cameras (Fig. 22) were used to take 2D PIV

with one being used for a view of the entire airfoil and the other zoomed in on the leading

edge. Both cameras were 1600 x 1200 resolution CCD cameras (PCO 1600, Cooke Corp).

The flow was seeded with 1~5 micron oil droplets while illumination was provided by a

double-pulsed Nd:YAG laser (NewWave Research Solo) adjusted on the second harmonic

and emitting two laser pulses at a wavelength of 532 nm at a repetition rate of 3 Hz. The laser

sheet was positioned and created by passing the laser beam through a laser arm and cylindrical lens an aligned with a mirror. The laser sheet was positioned near the center span of the model and had a thickness of approximately 2 mm. The triggering of the laser and camera was controlled via a digital delay generator (Berkeley Nucleonics, Model 565).

Figure 22: **Camera set-up** (*left camera for leading edge zoom view, right camera for entire airfoil view*)

Test Cases

Numerous test cases were run to better understand the extent in which dynamic roughness can be controlled. A Reynolds number study was conducted in which the incoming flow was set to 4 different speeds (2.7, 5.3, 7.8, and 10.4 m/s) resulting in chord Reynolds numbers of

25,000, 49,000, 73,000, and 97,000. This study showed how the angle of attack in which the clean (no dynamic roughness control activated) airfoil stalls and how much of an increase in angle of attack the dynamic roughness can achieve before stall.

A frequency study was conducted at an angle of attack of 14 degrees for a Reynolds number of 49,000. The pressure provided to the chamber was set to the highest possible which produced element heights of 195 when ran at a frequency of 30 Hz, 230 micron when ran at a frequency above 60 Hz, and heights between 195 and 230 micron between 30 and 60 Hz. The drive frequency was adjusted in 10 Hz increments down from 90 Hz until control was lost.

A combination of a height and frequency study was conducted as well at an angle of attack of 15 degrees for a Reynolds number of 73,000. Three frequencies (90, 60, and 30 Hz) were used, and the pressure supplied to the chamber was adjusted to obtain different roughness element heights. Due to the pressure being controlled by both the release valve and the drive frequency, it was difficult to obtain the same heights for each frequency, but enough were obtained to see how decreasing element height affects flow control.

Unfortunately, pressure data has not currently been obtained as there were leaks found in the leading edge pressure taps caused by the heating of the pressure chamber. A rebuild of the model and adding a heat exchanger to the actuation system will alleviate the problem in the future. For this reason, only PIV data is used to verify the existence of flow control suggest the increase of lifting performance. Most average cases of PIV data shown are based on 345 image pairs, but for those in which turbulent kinetic energy and vorticity are examined, there were 900 image pairs used.

Results and Discussion

Reynolds Number Study

Results from the Reynolds number study are shown in Figures 23-26. These contours of average velocity as well as arrows showing the average flow direction clearly show the ability for dynamic roughness to control flow in the low Reynolds number regime. Figures 23, 24, and 26 each start at the angle in which flow starts to separate without the dynamic roughness actuated and stop at the angle in which dynamic roughness no longer can control the flow well enough for complete attachment. Figure 25 starts at one angle of attack higher than the flow initially starts to separate. In each figure, the left images have the dynamic roughness turned off (Clean) and the right images have the dynamic roughness turned on (DR On) with the actuation frequency being 90 Hz and roughness height 230 micron. Preliminary numerical and computational results had shown that larger element height (as long as it is less than the boundary layer thickness) and higher actuation frequencies are more likely to control the flow; thus, it was decided to use the maximum drive frequency and roughness height possible.

For the lowest Reynolds number case of 25,000 (Fig. 23), the flow is able to increase the angle of attack approximately 2 degrees, from 10 degrees to 12 degrees, before the airfoil stalls. Even when the airfoil is in a deep stall, the dynamic roughness is able to thin the separation region in the vicinity of the leading edge. The stalling of the airfoil at this speed appears to be similar to that of a thin airfoil stall.

Approximately doubling the Reynolds number to 49,000 (Fig. 24) shows that the use of dynamic roughness increases the angle of attack range for attached flow by 3 degrees, from 13 to 16 degrees, before the airfoil goes into a deep stall. At an angle of attack of 15 degrees, the dynamic roughness is still able to control the flow across the upper surface of the airfoil, but a leading edge separation

bubble is present. For angles of attack below this, the flow is completely attached, and above 15 degrees, the bubble bursts causing complete separation.

At Reynolds numbers of 73,000 and 97,000 (Fig. 25 and 26 respectively), the dynamic roughness is able to increase the angle of attack range of attached flow by 3 degrees as well, but from 14 to 16 degrees as opposed to 13 to 15 degrees for the Re = 49,000 case. Comparing the two higher speed cases, they both have a relatively large separation bubble at 16 degrees, but the lower speed case (Fig. 25) has a thicker bubble. At 17 degrees, the lower Reynolds number case is in fully developed deep stall while the higher Reynolds number case has a very large separation bubble covering a distance of more than half the airfoil. Any slight disturbances will burst this bubble which makes it a very unstable flow condition.

In general, while within the low Reynolds number regime, the higher the Reynolds number, the higher the angle of attack at which a separation bubble will become present. The higher the Reynolds number, the smaller the separation bubble and the easier it is control the flow. These preliminary results have shown that at Reynolds numbers on the order of 50,000 to 100,000, dynamic roughness can generally increase the stall angle of a NACA 0012 airfoil by 3 degrees.

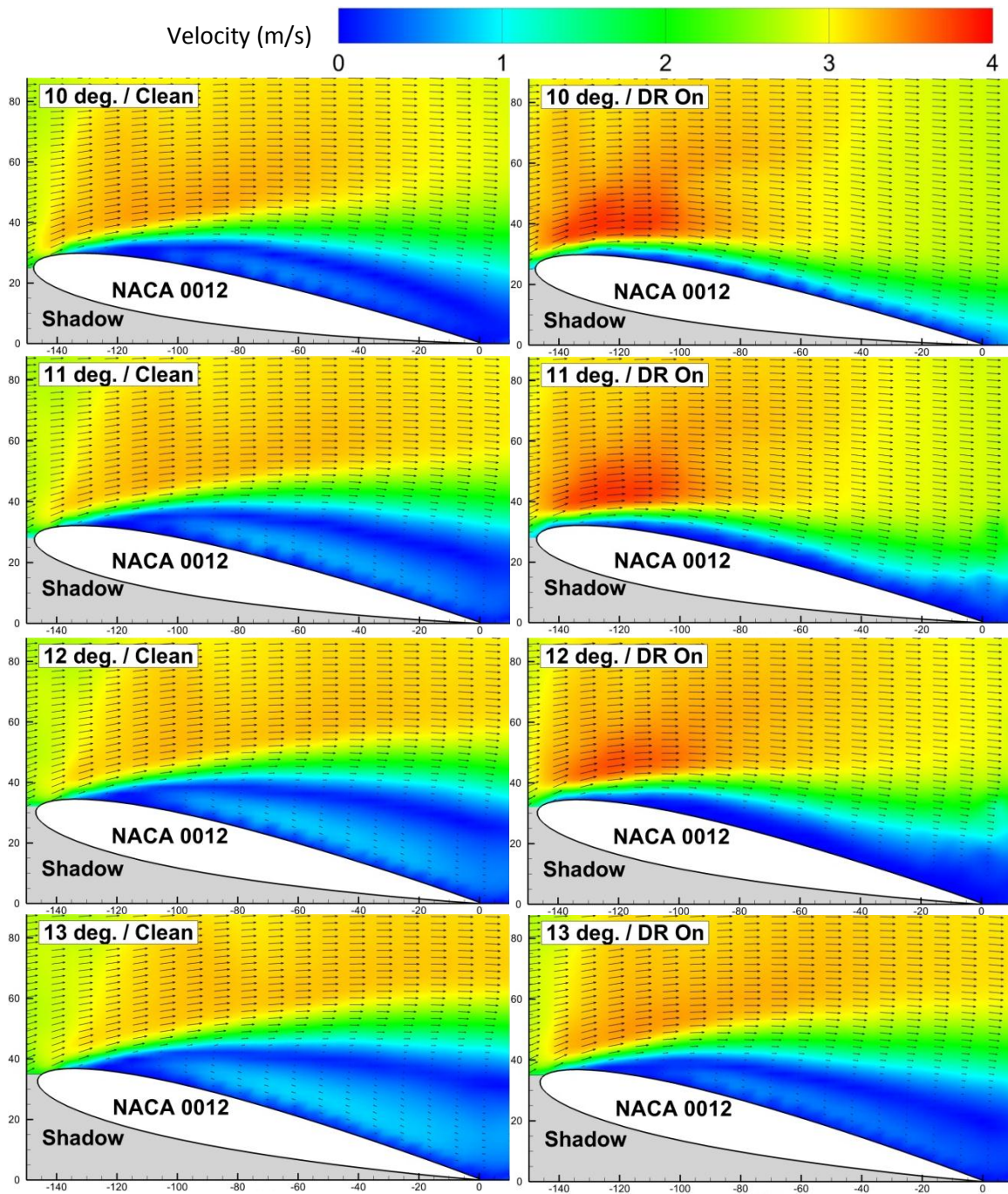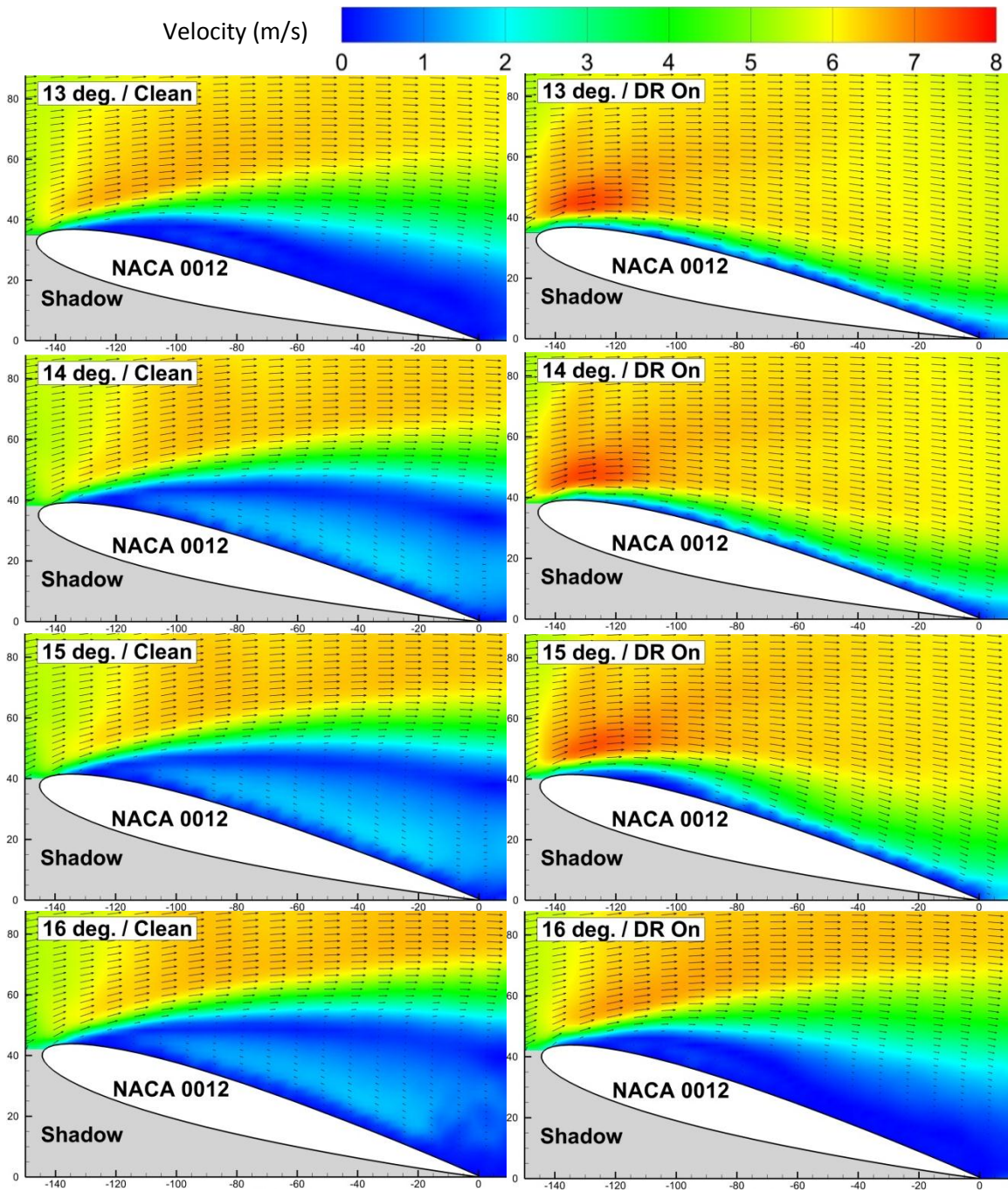**Figure 23:   Average velocity contours for $Re_c = 25,000$**

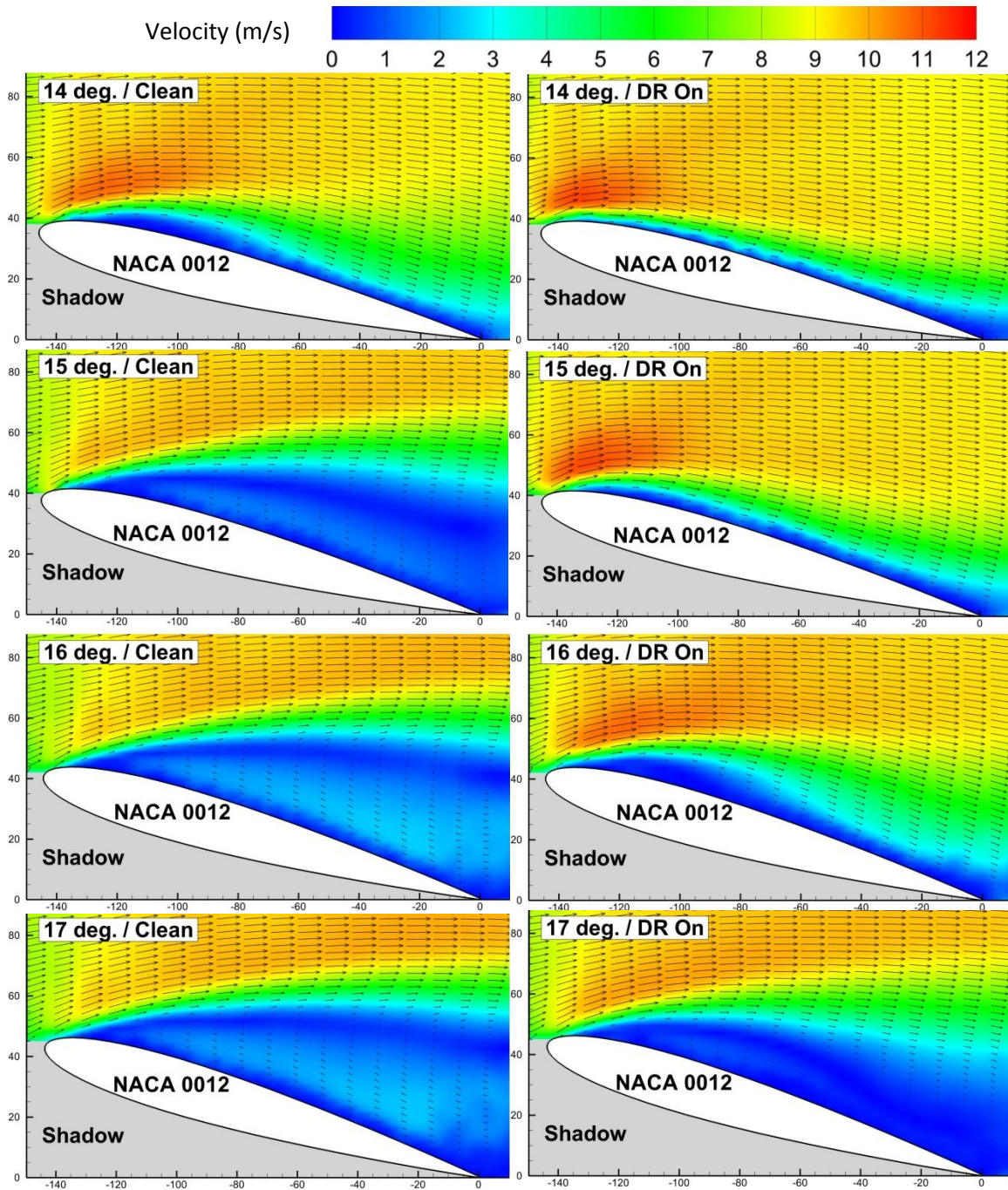**Figure 24: Average velocity contours for $Re_c = 49,000$**

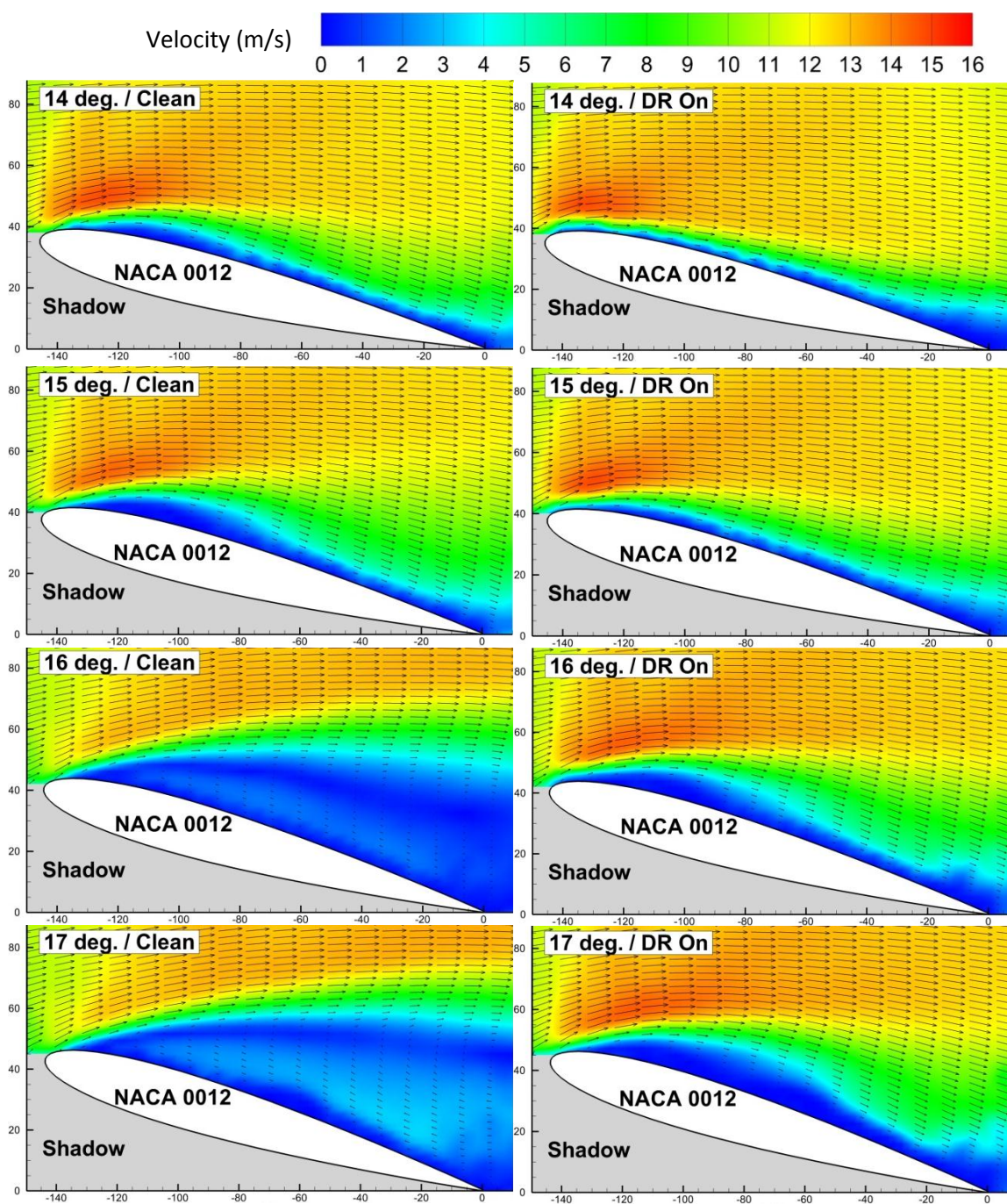**Figure 25:   Average velocity contours for $Re_c = 73,000$**

Figure 26: **Average velocity contours for Re$_c$ = 97,000**

Frequency Study

Results from the frequency study are shown in Figures 27 and 28 with the first figure showing the average velocity contours on the upper surface of the entire airfoil and the second being zoomed in on the leading edge. From these figures, it can be seen that at this set flow condition (Reynolds number = 49,000 and angle of attack = 14 degrees) that without the dynamic roughness actuating, the airfoil is in a fully developed deep stall. Once the roughness is actuated at or above a frequency of 50 Hz, the flow becomes reattached to the leading edge of the upper surface bringing the airfoil out of stall. At actuation frequencies at or below 40 Hz, the flow becomes separated putting the airfoil back into a stall configuration.

Examples of the average vorticity (Fig. 29 and 30) as well as turbulent kinetic energy (Fig. 31 and 32) were taken as part of the frequency study. For these, both the clean airfoil and highest frequency case are shown. From the vorticity images, it can be seen that when the flow is not controlled, there is a shear layer separating off of the leading edge. When the dynamic roughness is engaged, the boundary layer is kept attached to the leading edge with a large amount of vorticity in the region of and just downstream of the dynamic roughness. The TKE contours show that when the flow is separated from the airfoil, there is a large amount of TKE in the wake region of the airfoil as expected with very little near the leading edge. With the dynamic roughness actuated, there is large amount of turbulence directly above the dynamic roughness region which is assisting in reattaching the flow. This turbulence breaks down shortly after the dynamic roughness region, but reappears near the trailing edge. When the dynamic roughness is reattaching the flow at the leading edge, the airfoil begins to stall at this angle from the trailing edge which is causing the high levels of turbulence near the trailing edge for the attached case.

Figure 27: Average velocity contours (wide view) for different dynamic roughness control frequencies.
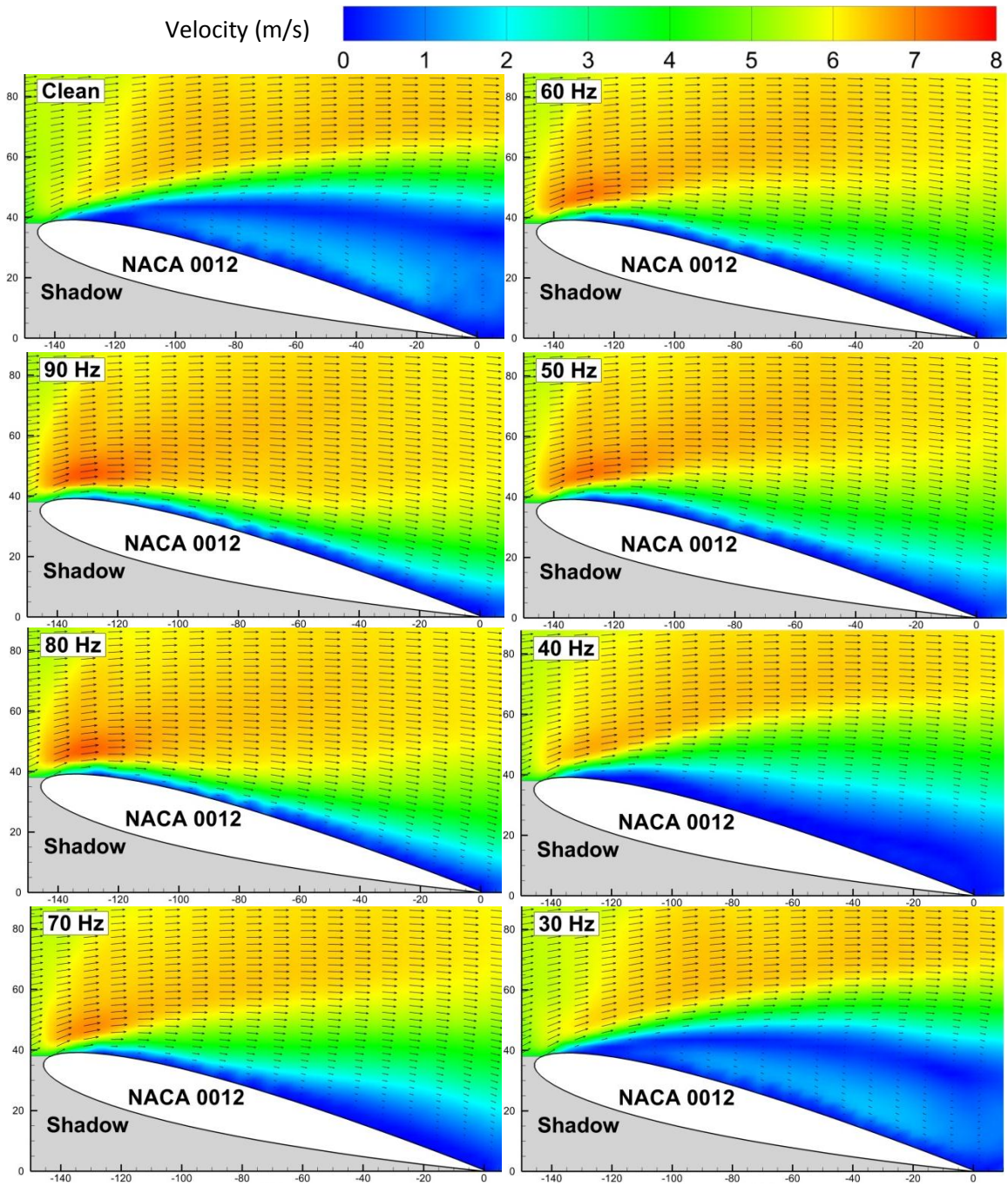
Angle of attack = 14°, Re_c = 49,000
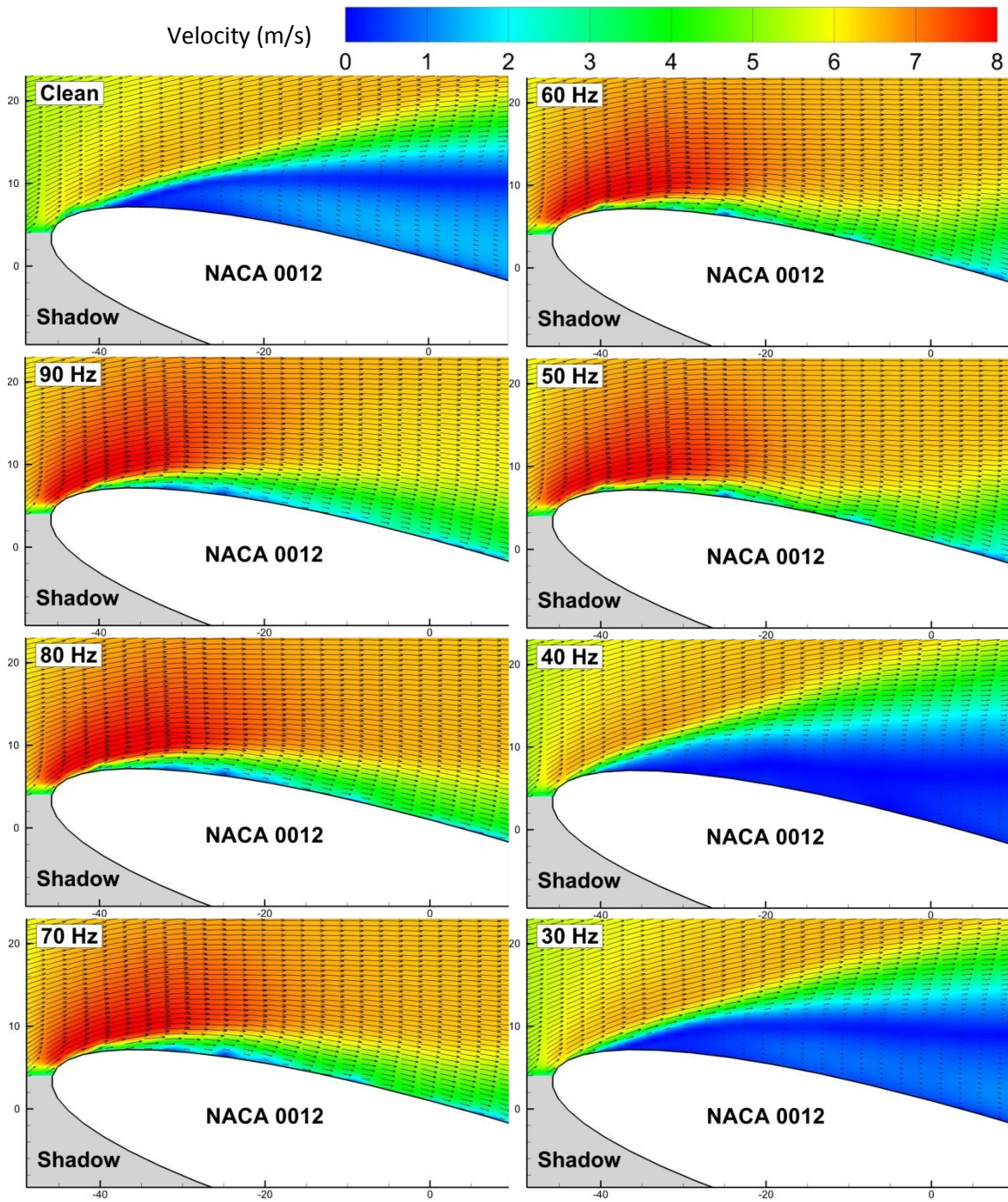
Figure 28: Average velocity contours (zoom view) for different dynamic roughness control frequencies.

Angle of attack = 14°, Re_c = 49,000

Figure 29: **Average vorticity contours for uncontrolled (clean) and controlled (90 Hz, 230 micron dynamic roughness) wide view**

Angle of attack = 14°, Re_c = 49,000

Figure 30:   Average vorticity contours for uncontrolled (clean) and controlled (90 Hz, 230 micron dynamic roughness) zoom view

Angle of attack = 14º, Re$_c$ = 49,000

Figure 31: Turbulent kinetic energy contours for uncontrolled (clean) and controlled (90 Hz, 230 micron dynamic roughness) wide view
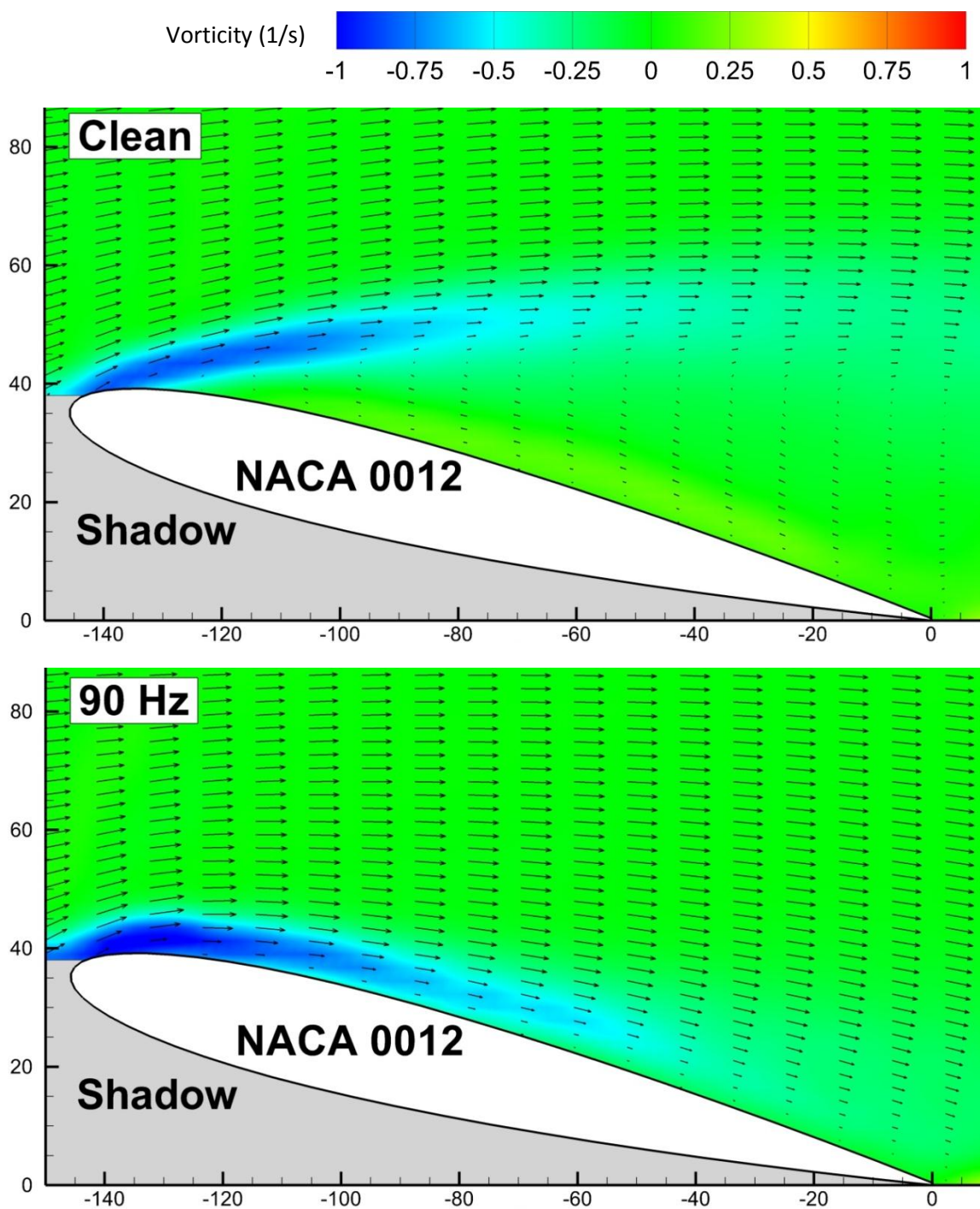
Angle of attack = 14º, Re_c = 49,000

Figure 32: **Turbulent kinetic energy contours for uncontrolled (clean) and controlled (90 Hz, 230 micron dynamic roughness) zoom view**

Angle of attack = 14°, Re_c = 49,000

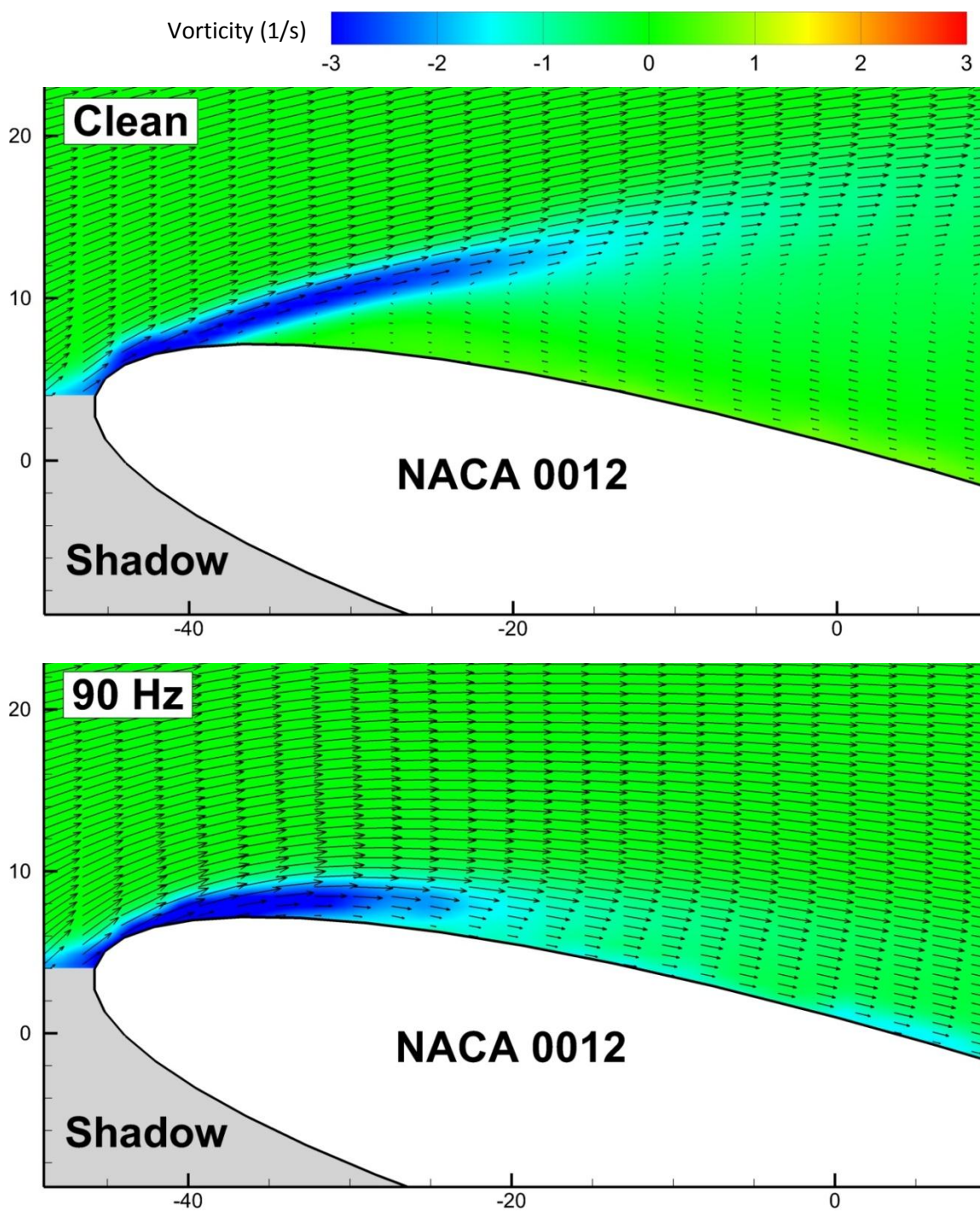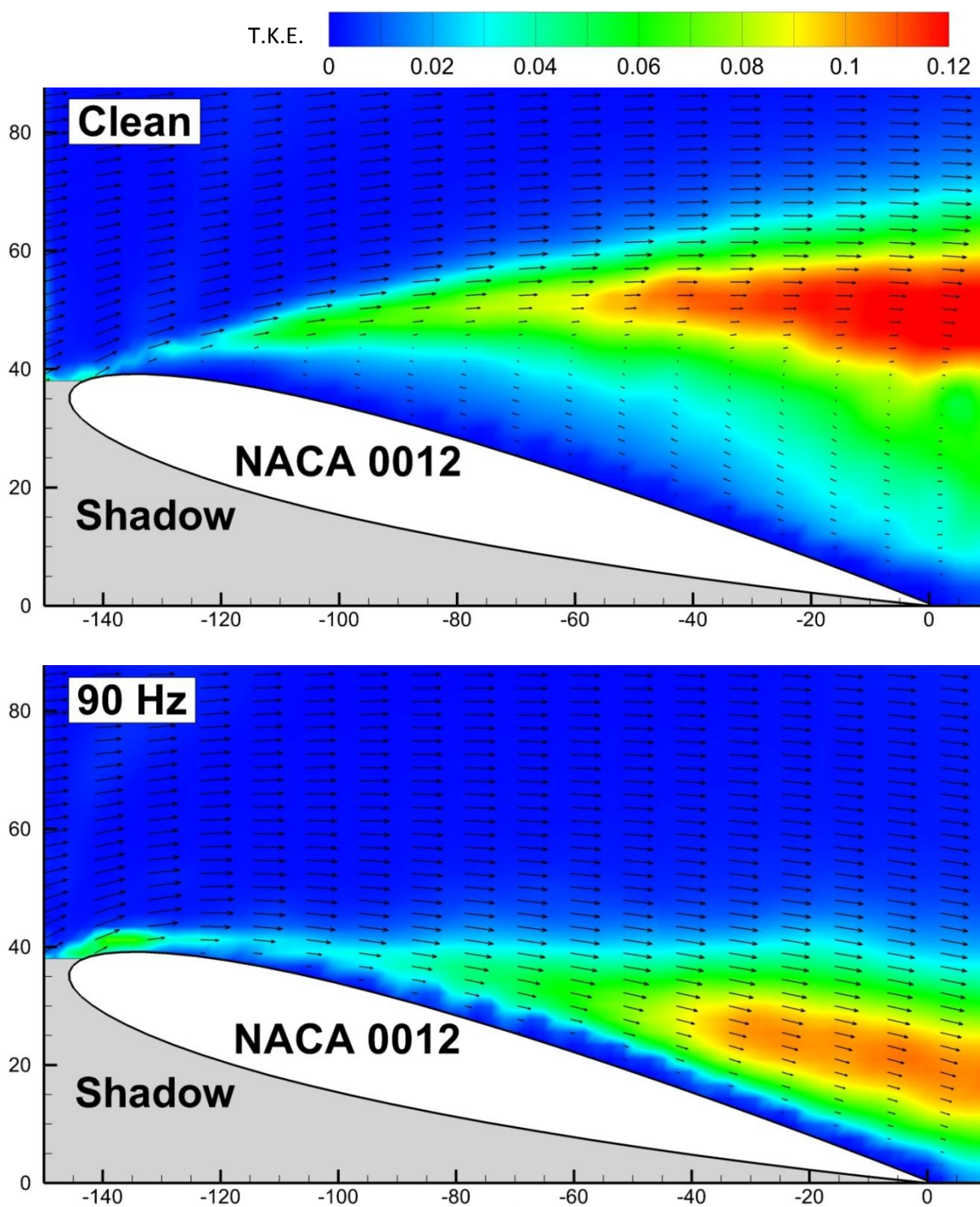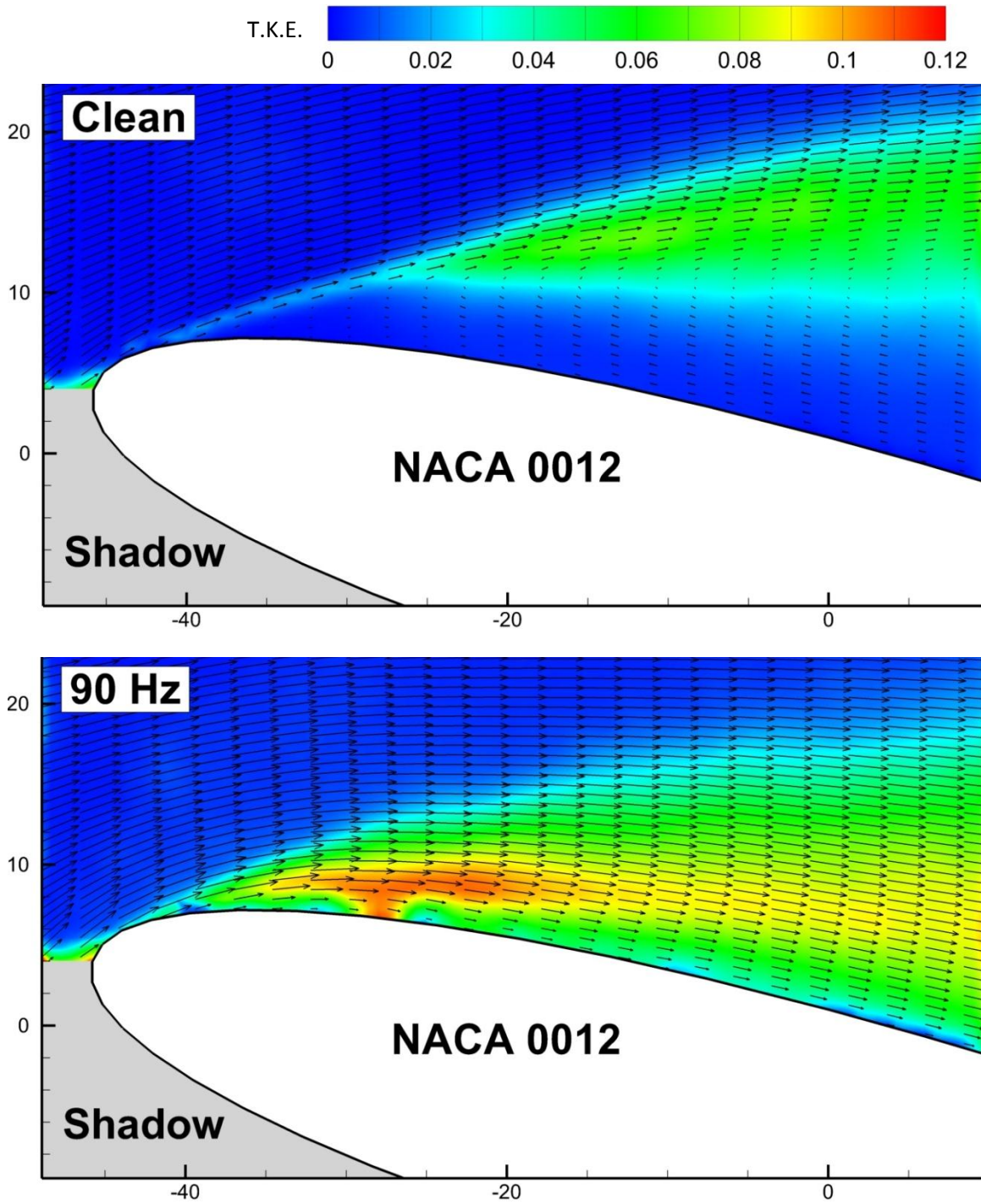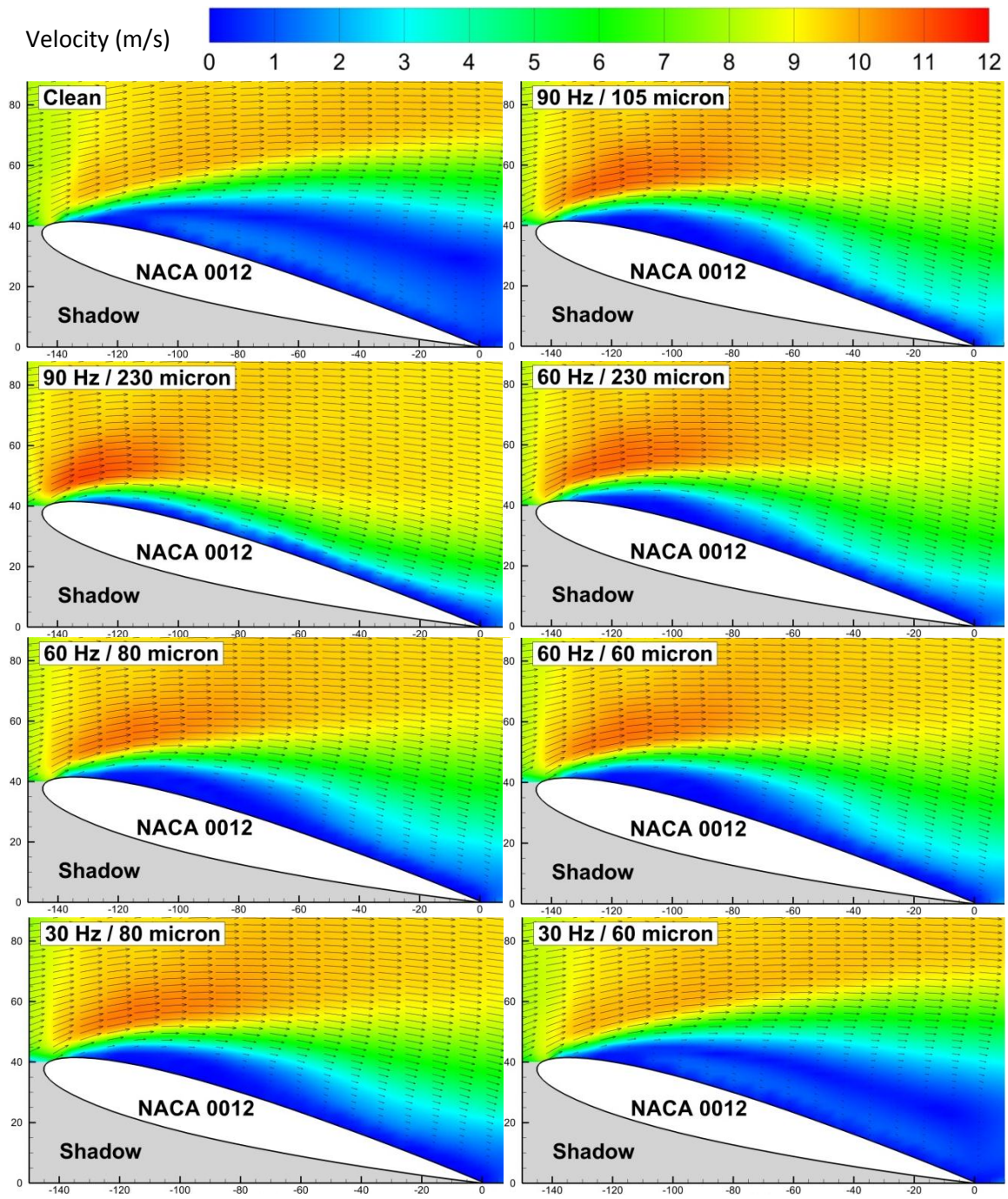**Roughness Height Study**

The results of the roughness height study are shown in Figure 33. Due to the difficulties in obtaining the same roughness heights at all frequencies, only a select few at different frequencies were chosen which demonstrate the effect of roughness element height on flow control. The frequency and height for each case are shown in the upper left corner of each image.

For dynamic roughness running at 90 Hz and the highest possible element height of 230 micron that was able to be produced, the flow is attached to the airfoil. Reducing the roughness height to 105 micron at that height allowed the formation of a leading edge separation bubble. Reducing the frequency to 60 Hz and increasing the roughness element height back to the maximum of 230 micron, produced similar results to that of the 90 Hz 105 micron case in which a leading edge separation bubble is present. Remaining at 60 Hz and reducing the element height to 80 and 60 micron increased the leading edge separation bubble size slightly as flow control is deteriorating.

Further reduction in the dynamic roughness actuation frequency to 30 Hz while maintaining element heights of 80 and 60 micron deteriorates the flow control until it is completely lost. The 30 Hz 80 micron case is slightly worse than the 60 Hz 60 micron case, but once the roughness height is decreased to 60 micron at this low of a frequency, all flow control is lost and the airfoil goes into a deep stall. In general, for a given frequency, increasing the roughness height will increase the ability for flow control as long as it is still shorter than the boundary layer thickness.

Figure 33:   Average velocity contours for roughness element height and frequency study

Angle of attack = 15°, Re_c = 73,000

Conclusion

An experimental investigation was performed on the performance of dynamic roughness as a flow control device to prevent the formation of a leading edge separation bubble at low Reynolds numbers. It was found that the higher the frequency the further the dynamic roughness could be used as a flow control device. At a given frequency, the taller the roughness element height the increased ability to obtain flow control as long as the roughness height is shorter than the local boundary layer thickness. Dynamic roughness can greatly increase the angle at which an airfoil will stall and suggest an increase in the lifting performance. Further research is needed to quantify how much more lift can be generated as well as the power consumption for dynamic roughness.

Chapter 4) Conclusion

Two experimental investigations were performed on surface actuation devices which suppress the formation of the leading edge separation bubble at low Reynolds numbers. These devices have shown that both two-dimensional (burst control plate) and three-dimensional (dynamic roughness) surface actuation devices are capable of delaying stall on a NACA 0012 airfoil. The ability to delay stall through the use of these devices allows for a further increase in lift performance for lifting surfaces.

It has been found that the higher the frequency an actuation device operates, the more likely it will be able to prevent flow separation. Displacement height of the actuation device is a significant parameter in the ability to use such devices for flow control. Displacement heights that are larger than the local boundary layer thickness will not work as well at reattaching a boundary layer as those that are a fraction of the size of the boundary layer thickness. Displacement heights that are greatly shorter than that of the boundary layer thickness require much higher actuation frequencies than those that are taller.

Further research is needed to investigate the feasibility of these surface actuation devices for flow control devices. The increased amount of lift needs to be compared to the amount of power needed to operate these devices. A study on the effects of drag at these higher angles of attack also needs to be conducted to ensure that the lift to drag ratio is not being greatly worsened. Future work can also be performed on how much of an effect element arrangement, orientation, and whether 2D or 3D actuation devices are more effective. The finding of a passive surface actuation system which would react to the need for flow control to be activated as well as not require any power input would be greatly beneficial for advancement of flight vehicles.

Bibliography

[1]Tani, I., 1964, "Low Speed Flows Involving Bubble Separations," *Prog. Aeronaut. Sci.*, Vol. 5, pp. 70–103.

[2]Carmichael, B. H., 1981, "Low Reynolds Number Airfoil Survey," *NASA CR-165803*, Vol. 1.

[3]Lissaman, P. B. S., 1983, "Low-Reynolds-Number Airfoils," *Annual Review of Fluid Mechanics*, Vol. 15, pp.223–239.

[4]J. T. Mueller, ed., 2001, "Fixed and Flapping Wing Aerodynamics for Micro Air Vehicle Applications," *Progress in Astronautics and Aeronautics*, Vol. 195, AIAA.

[5]Gad-el-Hak, M. 2001, "Micro-Air-Vehicles: Can They be Controlled Better," *Journal of Aircraft*, Vol. 38, No. 3, pp. 419-429.

[6]FItzgerald, E. J., and Mueller, T. J., 1990, "Measurements in a Separation Bubble on an Airfoil Using Laser Velocimetry," AIAA J., 28_4_, pp. 584–592.

[7]Brendel, M., and Mueller, T. J., 1987, "Boundary Layer Measurements on an Airfoil at Low Reynolds Numbers," AIAA Paper No. 87-0495.

[8]O'Meara, M. M., and Mueller, T. J., 1987, "Laminar Separation Bubble Characteristics on an Airfoil at Low Reynolds Numbers," AIAA J., 25_8_, pp. 1033–1041.

[9]Lang, M., Rist, U., and Wagner, S., 2004, "Investigations on Controlled Transition Development in a Laminar Separation Bubble by Means of LDA and PIV," *Exp. Fluids*, 36, pp. 43–52.

[10]Ol, M. V., Hanff, E., McAuliffe, B., Scholz, U., and Kaehler, C., 2005, "Comparison of Laminar Separation Bubble Measurements on a Low Reynolds Number Airfoil in Three Facilities," 35th AIAA Fluid Dynamics Conference and Exhibit, Toronto, Ontario, June 6–9, AIAA Paper 2005-5149.

[11]Raffel, M., Favier, D., Berton, E., Rondot, C., Nsimba, M., and Geissler, M., 2006 "Micro-PIV and ELDVWind Tunnel Investigations of the Laminar Separation Bubble Above a Helicopter Blade Tip," *Meas. Sci. Technol*., 17, pp. 1652–1658.

[12]Burgmann, S., Brücker, S., Schröder, W., 2006, "Scanning PIV Measurements of a Laminar Separation Bubble," *Exp. Fluids*, 41, pp. 319–326.

[13]Rinoie, Okuno, andSunada, "Airfoil Stall Suppression by Use of a Bubble Burst Control Plate", AIAA Journal Vol. 47, No. 2, Feb. 2009.

[14]Gall, Huebsch, and Rothmayer, 2010, "Dynamic Roughness as a Means of Leading Edge Separation Flow Control," *27th International Congress of the Aeronautical Sciences.*